UNIVERSITY OF
Southampton
Institute of Sound and
Vibration Research

ISVR Technical Memorandum

Validation of coupled Waveguide Finite Element-Wavedomain Boundary Element (WFBE) method for the case of an infinite plate strip

I. Prasetiyo, D.J. Thompson and J. Ryue

ISVR Technical Memorandum 997

October 2012

SCIENTIFIC PUBLICATIONS BY THE ISVR

Technical Reports are published to promote timely dissemination of research results by ISVR personnel. This medium permits more detailed presentation than is usually acceptable for scientific journals. Responsibility for both the content and any opinions expressed rests entirely with the author(s).

Technical Memoranda are produced to enable the early or preliminary release of information by ISVR personnel where such release is deemed to the appropriate. Information contained in these memoranda may be incomplete, or form part of a continuing programme; this should be borne in mind when using or quoting from these documents.

Contract Reports are produced to record the results of scientific work carried out for sponsors, under contract. The ISVR treats these reports as confidential to sponsors and does not make them available for general circulation. Individual sponsors may, however, authorize subsequent release of the material.

UNIVERSITY OF SOUTHAMPTON
INSTITUTE OF SOUND AND VIBRATION RESEARCH
DYNAMICS GROUP

Validation of coupled Waveguide Finite Element-Wavedomain Boundary Element (WFBE) method for the case of an infinite plate strip

by

I. Prasetiyo, D.J. Thompson and J. Ryue

October 2012

ISVR Technical Memorandum No. 997

Authorised for issue by
Prof. D.J. Thompson

Abstract

The purpose of the work reported here is to validate and verify results obtained using the Waveguide Finite Element and Wavedomain Boundary Element (WFBE) method using the software WANDS. This study concerns the vibro-acoustic behaviour of a plate strip in terms of its mobility, sound radiation and transmission loss. Moreover, it aims to provide a basis for employing the method in more complicated cases.

The plate strip is assumed to be infinite in length but have a finite width where it is confined by parallel boundaries. Simply supported boundaries are considered, allowing ready comparison with analytical results. The comparisons between the analytical results and the numerical ones show that WFBE is applicable for investigating the waveguide structure behaviour. However, some practical aspects of implementing this method using the WANDS software should be borne in mind in order to obtain correct results. Firstly, the Waveguide Boundary Element (WBE) mesh must have a closed boundary. Secondly, for comparison with the analytical results, a finite rigid baffle needs to be included in the model by extending the length of the WBE fluid model beyond the width of the structure. Thirdly, in the current implementation of WANDS it is better to use solid elements rather than plates for calculating cases incorporating the WFE-WBE coupling, e.g. the radiated power and the transmission loss. This latter aspect could be dealt with by improvements to the software.

Contents

Acknowledgements

The first author is grateful to Directorate General of Higher Education (DGHE), Department of National Education of Indonesia for providing a postgraduate scholarship.

1. Introduction

A “waveguide structure” is one which is long (or infinite) in one (or more) dimensions and has a constant cross-section perpendicular to this axis. The Waveguide Finite Element (WFE) method [1] is a useful approach to calculate the dynamic behaviour of such a waveguide structure in an efficient way. This approach uses a two-dimensional finite element mesh with special elements that allow for wave propagation in the third dimension. The general three-dimensional solution can be obtained from an inverse Fourier transform over wavenumber. For the case of the sound radiation prediction, the coupled Waveguide Finite Element-Boundary Element (WFBE) method can be used to calculate the interaction with the acoustic field [2, 3]. The method can be used for many such structures which have a constant geometry along one direction and therefore form a waveguide, for example railway tracks [2, 4, 5], pipes [6] and tyres [1, 7]. Acoustic transmission through panels can also be considered.

The WANDS software [8, 9] has been developed at ISVR to implement the WFBE method. It includes structural beam, plate and solid elements, acoustic finite elements, and boundary elements for both acoustic and solid domains.

For the particular case of sound radiation and transmission involving the coupling between structural components and the surrounding air, analytical models have been developed [10] to enable validation of the WFBE approach. These are based on an infinite plate strip with simply supported boundaries. Results have been given in [10] for the mobility, the sound radiation due to a point force and the sound transmission due to an incident sound field.

In this report, validation of the numerical model is conducted by comparing the results from WANDS with those from the analytical models. Comparisons of the results of the two methods as well as various methods for evaluating the integral in the inverse Fourier transform are discussed in detail. This step is important to know the effect of discretization in wavenumber space in terms of step size and wavenumber range in order to avoid losing information. As the numerical model is implemented with a finite baffle, the effect of baffle width on the accuracy of the radiated power calculation is also investigated. Moreover, the thickness (or depth) of the WBE mesh is considered to avoid the WBE method produces unreliable results

[11] owing to a close distance between the opposite sides of the mesh. In general, the verification of the numerical result by comparison with the analytical one is of importance as a prerequisite to employing the method in more complicated cases.

2. Waveguide Finite Element method

A structure with uniform geometrical and material properties along one direction but arbitrary cross-section can be modelled numerically using the waveguide finite element (WFE) method [3, 12, 13]. Under this formulation, the structural behaviour is treated as a two-dimensional problem in which the waveguide cross-section in the $y-z$ plane is discretized into a number of finite elements. In the other dimension, taken here as the $x-$direction, the structure has homogeneous properties and harmonic wave solutions of the form $e^{-i\kappa x}$ are assumed. Therefore, a solution is obtained which is three-dimensional in nature, without requiring a three-dimensional model as would be required using conventional finite elements for a similar outcome. This situation offers a versatile and numerically efficient method for such structures, especially when they are long (or effectively infinite) in the $x-$direction.

2.1 Plate elements

Consider a plate strip element with translational displacements u, v and w in the x, y and z directions and a rotational displacement ϕ about the x axis, as shown in Figure 2.1. The element is defined by node points in the $y-z$ plane which become lines in the $x-$direction. This basic element is employed in the WFE formulation to build up any thin-walled complex structure. Derivation of the equations of motion for each element under the WFE formulation can be found in [3, 13, 14]. Harmonic motion at frequency ω is assumed throughout. For a structure assembled of a number of elements, the overall equation can be written in the form

$$\left[\sum_{n=0}^{4}\mathbf{K}_n\frac{\partial^n}{\partial x^n}-\omega^2\mathbf{M}\right]\mathbf{W}(x)=\mathbf{F}(x) \tag{2.1}$$

where $\mathbf{K}_n$ and $\mathbf{M}$ are stiffness and mass matrices which correspond to elastic energy in the system and kinetic energy of the structure respectively. $\mathbf{W}$ is the vector of

nodal displacement amplitudes at nodes in the $y-z$ plane which is sought as the solution and **F** is a vector of nodal force amplitudes. **W** is also a function of ω (suppressed for clarity). In the numerical implementation, the plate strip element includes in-plane and out-of plane motion so that the displacements are given by $\mathbf{W}(x)=\begin{bmatrix} u_1 & v_1 & w_1 & \phi_1 & u_2 & v_2 & w_2 & \phi_2 \end{bmatrix}^{\mathbf{T}}$.

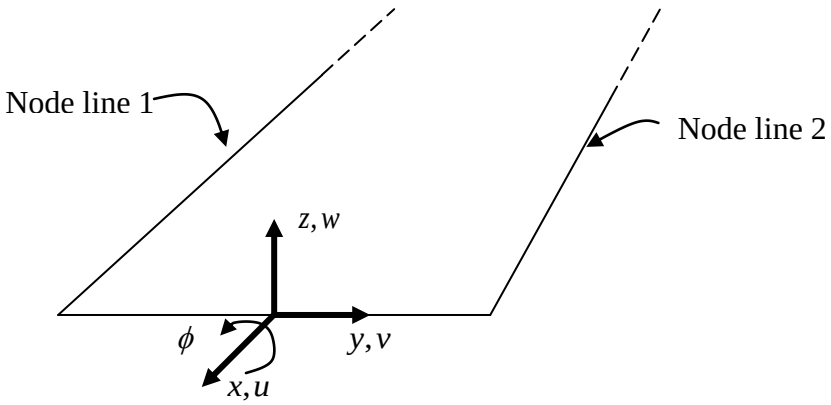

Figure 2.1. A shell (or plate) strip element

For clarity, Eq. (2.1) can be expanded as follows

$$\left[\mathbf{K}_4\frac{\partial^4}{\partial x^4}+\mathbf{K}_2\frac{\partial^2}{\partial x^2}+\mathbf{K}_1\frac{\partial}{\partial x}+\mathbf{K}_0-\omega^2\mathbf{M}\right]\mathbf{W}(x)=\mathbf{F}(x) \tag{2.2}$$

Note that the term $\mathbf{K}_3$ is not usually present. The matrices $\mathbf{K}_4$, $\mathbf{K}_2$, $\mathbf{K}_0$ and **M** are symmetric while $\mathbf{K}_1$ is skew-symmetric. Plate out-of-plane bending motion contributes terms in $\mathbf{K}_4$, $\mathbf{K}_2$ and $\mathbf{K}_0$ while in-plane motion contributes terms in $\mathbf{K}_2$, $\mathbf{K}_1$ and $\mathbf{K}_0$. The matrices $\mathbf{K}_n$ and **M** are derived in [9] in terms of the dimensions and material properties of the element.

For the case of an infinite structure, a spatial Fourier transform in the longitudinal direction enables the response of the structure to be obtained. The following Fourier transform pair is used

$$\tilde{\mathbf{W}}(\kappa)=\int_{-\infty}^{\infty}\mathbf{W}(x)e^{i\kappa x}dx \tag{2.3}$$

$$\mathbf{W}(x)=\frac{1}{2\pi}\int_{-\infty}^{\infty}\tilde{\mathbf{W}}(\kappa)e^{-i\kappa x}d\kappa \tag{2.4}$$

and a similar transform for $\mathbf{F}$. Taking the Fourier transform of Eq. (2.2), to transform it from the spatial domain into the wavenumber domain, yields

$$\left[\mathbf{K}_4(-i\kappa)^4+\mathbf{K}_2(-i\kappa)^2+\mathbf{K}_1(-i\kappa)+\mathbf{K}_0-\omega^2\mathbf{M}\right]\tilde{\mathbf{W}}(\kappa)=\tilde{\mathbf{F}}(\kappa) \tag{2.5}$$

where κ is the wavenumber in the $x-$direction.

2.2 Solid elements

Similarly a solid element can be defined by four (or more) node points. Nodes in the solid elements have 3 degrees of freedom corresponding to three translational displacements. Using the same principle as presented in section 2.1, the overall motion of a structure built up of solid elements can be written as follows [9]

$$\left[\mathbf{K}_2\frac{\partial^2}{\partial x^2}+\mathbf{K}_1\frac{\partial}{\partial x}+\mathbf{K}_0-\omega^2\mathbf{M}\right]\mathbf{W}(x)=\mathbf{F}(x) \tag{2.6}$$

where again $\mathbf{W}$ is also a function of ω (suppressed for clarity). Taking Fourier transforms, this gives

$$\left[\mathbf{K}_2(-i\kappa)^2+\mathbf{K}_1(-i\kappa)+\mathbf{K}_0-\omega^2\mathbf{M}\right]\tilde{\mathbf{W}}(\kappa)=\tilde{\mathbf{F}}(\kappa) \tag{2.7}$$

where κ is the wavenumber in the $x-$direction. The matrices $\mathbf{K}_2$, $\mathbf{K}_1$, $\mathbf{K}_0$ and $\mathbf{M}$ are stiffness and mass matrices as before, and are given in [9].

2.3 Free wave solution

Setting the external force $\tilde{\mathbf{F}}=\mathbf{0}$ leads to the free vibration case, which results in a twin-parameter eigenvalue problem where both wavenumber κ and frequency ω are unknown:

$$\left[\mathbf{K}_4(-i\kappa)^4+\mathbf{K}_2(-i\kappa)^2+\mathbf{K}_1(-i\kappa)+\mathbf{K}_0-\omega^2\mathbf{M}\right]\tilde{\mathbf{W}}=\mathbf{0} \tag{2.8}$$

This is a linear eigenvalue problem in squared frequency ω^2 for a given wavenumber κ. Alternatively the polynomial eigenvalue problem in wavenumber κ can be solved for a given frequency ω. The solution obtained can then be used to describe the dispersion characteristics of the structure while the corresponding eigenvectors represent the cross-section deformation modes. For the case of $\kappa = 0$, the eigenvalue problem reduces to

$$\left[\mathbf{K}_0 - \omega^2 \mathbf{M}\right]\tilde{\mathbf{W}} = \mathbf{0} \tag{2.9}$$

where the frequencies that are the solution of Eq. (2.9) are the cut-on frequencies of the various waves in the waveguide. Otherwise, however, Eq. (2.8) is a non-standard eigenvalue problem in wavenumber which can be more efficiently solved if it is transformed into a standard form. This can be achieved by transforming Eq. (2.8) so that the unknown eigenvalue κ does not appear in the system matrix. The following procedure is used for solving such an eigenvalue problem by transforming it into a standard eigenvalue problem form for $(-i\kappa)^{-1}$ as given by Gavric [13]. The procedure starts by inverting the part of Eq. (2.8) which does not depend on wavenumber, $\left(\mathbf{K}_0 - \omega^2 \mathbf{M}\right)$. Eq. (2.8) is then multiplied by the inverted matrix and divided by $-i\kappa$ to give the following relation

$$\left(\mathbf{A_1} + (-i\kappa)\mathbf{A_2} + (-i\kappa)^3 \mathbf{A_4}\right)\tilde{\mathbf{W}} = \frac{1}{(-i\kappa)}\tilde{\mathbf{W}} \tag{2.10}$$

where $\mathbf{A}_j = -\left(\mathbf{K_0} - \omega^2 \mathbf{M}\right)^{-1}\mathbf{K}_j$, $j = 1,\ 2,\ 4$. Eq. (2.10) can then be converted to a simple eigenvalue problem by adding three identities $(-i\kappa)^{j-1}\tilde{\mathbf{W}} = (i/\kappa)(-i\kappa)^j \tilde{\mathbf{W}}$ for $j = 1,\ 2,\ 3$ to yield the square matrix system

$$\begin{pmatrix} \mathbf{A_1} & \mathbf{A}_2 & \mathbf{0} & \mathbf{A}_4 \\ \mathbf{I} & \mathbf{0} & \mathbf{0} & \mathbf{0} \\ \mathbf{0} & \mathbf{I} & \mathbf{0} & \mathbf{0} \\ \mathbf{0} & \mathbf{0} & \mathbf{I} & \mathbf{0} \end{pmatrix} \begin{pmatrix} \tilde{\mathbf{W}} \\ (-i\kappa)\tilde{\mathbf{W}} \\ (-i\kappa)^2\tilde{\mathbf{W}} \\ (-i\kappa)^3\tilde{\mathbf{W}} \end{pmatrix} = \frac{1}{(-i\kappa)} \begin{pmatrix} \tilde{\mathbf{W}} \\ (-i\kappa)\tilde{\mathbf{W}} \\ (-i\kappa)^2\tilde{\mathbf{W}} \\ (-i\kappa)^3\tilde{\mathbf{W}} \end{pmatrix} \tag{2.11}$$

where $\mathbf{I}$ is the identity matrix. The dimension of the unknown eigenvector is four times the dimension of the original finite element model. The eigenvalues are the inverse of the wavenumbers $(-i\kappa)^{-1}$. Eq. (2.11) satisfies the standard eigenvalue problem form. For the case of $\mathbf{K}_4 = \mathbf{0}$, i.e. solid elements, Eq. (2.11) reduces to

$$\begin{pmatrix} \mathbf{A_1} & \mathbf{A}_2 \\ \mathbf{I} & \mathbf{0} \end{pmatrix} \begin{pmatrix} \tilde{\mathbf{W}} \\ (-i\kappa)\tilde{\mathbf{W}} \end{pmatrix} = \frac{1}{(-i\kappa)} \begin{pmatrix} \tilde{\mathbf{W}} \\ (-i\kappa)\tilde{\mathbf{W}} \end{pmatrix} \tag{2.12}$$

where $\mathbf{A}_j = -\left(\mathbf{K_0} - \omega^2\mathbf{M}\right)^{-1}\mathbf{K}_j$, $j = 1,\ 2$.

2.4 Forced response

In order to predict the forced response of a structure, all the wave solutions including nearfield waves are required. Hence, Eq. (2.11) and Eq. (2.12) have to be solved to obtain all wavenumbers and mode shapes at a given frequency ω.

For the case of forced vibration due to a concentrated load at a given frequency ω, the force can be represented using a delta function in the spatial domain as follows

$$\mathbf{F}(x) = \hat{\mathbf{F}}\delta\left(x\right) \tag{2.13}$$

where $\hat{\mathbf{F}}$ represents the nodal force vector. The response of the structure is then given as the solution to

$$\left[\mathbf{K}_4 \frac{\partial^4}{\partial x^4} + \mathbf{K}_2 \frac{\partial^2}{\partial x^2} + \mathbf{K}_1 \frac{\partial}{\partial x} + \mathbf{K}_0 - \omega^2\mathbf{M}\right]\mathbf{W}(x) = \hat{\mathbf{F}}\delta\left(x\right) \tag{2.14}$$

Using Fourier transforms as in Eq. (2.3), Eq. (2.14) is subsequently written as

$$\left[\mathbf{K}_4(-i\kappa)^4 + \mathbf{K}_2(-i\kappa)^2 + \mathbf{K}_1(-i\kappa) + \mathbf{K}_0 - \omega^2\mathbf{M}\right]\tilde{\mathbf{W}}(\kappa) = \tilde{\mathbf{F}}(\kappa) \tag{2.15}$$

where

$$\tilde{\mathbf{F}}\left(\kappa\right) = \int_{-\infty}^{\infty} \hat{\mathbf{F}}\delta(x)e^{i\kappa x}dx = \hat{\mathbf{F}} \tag{2.16}$$

and $\tilde{\mathbf{W}}(\kappa)$ is the displacement of the cross-section at wavenumber κ. By inverting the dynamic stiffness matrix in Eq. (2.15), the displacement of the structure in the wavenumber domain can be obtained

$$\tilde{\mathbf{W}}(\kappa) = \left[\mathbf{K}_4(-i\kappa)^4 + \mathbf{K}_2(-i\kappa)^2 + \mathbf{K}_1(-i\kappa) + \mathbf{K}_0 - \omega^2\mathbf{M}\right]^{-1} \tilde{\mathbf{F}}(\kappa) \qquad (2.17)$$

Subsequently, the displacement in the spatial domain can be recovered through the inverse Fourier transform, Eq. (2.4). This equation can be solved by several methods as discussed below.

2.5 Residue calculus method

Using the residue calculus method, as presented in [1, 2, 14, 15], the integral in Eq. (2.4) with limits $\pm\infty$ can be replaced by a contour integral in the complex plane. Two such curves are shown in Figure 2.2. For $x \leq 0$ the integral in Eq. (2.4) is performed over the upper half plane because the integrand will approach zero in this plane as $R \to \infty$. Similarly for $x > 0$ the integral is performed over the lower half plane. The integral is equal to $\pm 2\pi i$ times the sum of the residues at the poles of the integrand [16]

$$\oint \frac{f(z)}{q(z)} dz = 2\pi i \sum_p \frac{f(z)}{q'(z)} \qquad (2.18)$$

where $f(z)$ and $q(z)$ are finite functions of the complex variable z. Eq. (2.18) has poles, where the dynamic stiffness has zero determinant, at precisely the solutions to Eq. (2.8), i.e. the free wave solutions. It is assumed that each of them is a simple pole hence there are no duplicate wave solutions.

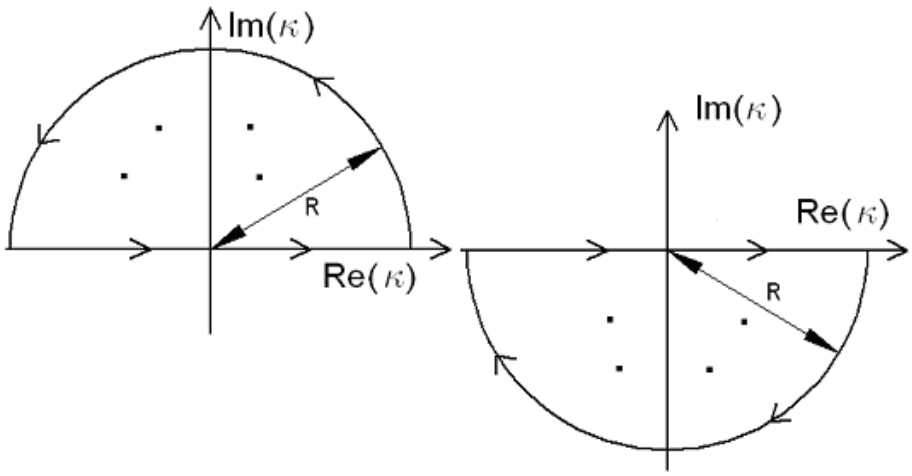

Figure 2.2. Path of integration in complex plane [1].

The response in the spatial domain is then calculated as a sum of residues as follows [1, 14]

$$W_{DOF}(x) = i\sum_{p} \frac{\tilde{\mathbf{W}}_{p,L}^{T}\tilde{\mathbf{F}}}{\tilde{\mathbf{W}}_{p,L}^{T}\left[\frac{\partial}{\partial\kappa}\left(\sum_{j}\mathbf{K}_{j}(-i\kappa)^{j}\right)_{\kappa=\kappa_p}\right]_{p}\tilde{\mathbf{W}}_{p,R}}\tilde{W}_{DOF,p,R} \tag{2.19}$$

where p is the number of waves in the structure under consideration at a given frequency. $\tilde{\mathbf{W}}_L$ and $\tilde{\mathbf{W}}_R$ are referred to as the left and right eigenvectors of Eq. (2.8) respectively for the eigenproblem evaluated at $\kappa = \kappa_p$. The DOF subscript is an index indicating the degree of freedom at which the displacement is required while $\tilde{W}_{DOF,p,R}$ is the component of the right eigenvector $\tilde{\mathbf{W}}_R$ corresponding with index DOF.

The differential term in the denominator of Eq. (2.19) can be derived as follows

$$\frac{\partial}{\partial\kappa}\left(\sum_{j}\mathbf{K}_{j}(-i\kappa)^{j}\right)_{\kappa=\kappa_p} = -i\left(4\mathbf{K}_{4}(-i\kappa)^{3} + 2\mathbf{K}_{2}(-i\kappa) + \mathbf{K}_{1}\right)_{\kappa=\kappa_p} \tag{2.20}$$

For the case of the solid elements, where $\mathbf{K}_4$ is absent, Eq. (2.20) becomes

$$\frac{\partial}{\partial \kappa}\left(\sum_j \mathbf{K}_j(-i\kappa)^j\right)_{\kappa=\kappa_p} = -i\left(2\mathbf{K}_2(-i\kappa)+\mathbf{K}_1\right)_{\kappa=\kappa_p} \tag{2.21}$$

2.6 Numerical integration

Aside from the residue calculus approach, the integration in Eq. (2.4) can also be solved for a limited wavenumber range by using a simple numerical integration technique such as the rectangle method [16]. This method works by dividing the area under the graph of Eq. (2.17) into r rectangles. The area of each is the product of height and width. Thus the integral in Eq. (2.4) becomes

$$\begin{aligned}\mathbf{W}(x) &= \frac{1}{2\pi}\int_{-\kappa_{\max}}^{\kappa_{\max}} \tilde{\mathbf{W}}(\kappa)e^{-i\kappa x}d\kappa \\ &\approx \frac{1}{2\pi}\sum_r \underbrace{\tilde{\mathbf{W}}(\kappa)}_{(1)}e^{-i\kappa x}\underbrace{\Delta\kappa}_{(2)}\end{aligned} \tag{2.22}$$

where term (1) determines the height of the rectangles and term (2), $\Delta\kappa$, is the step size, which is taken as an equal sub-division of the length. Figure 2.3 illustrates how this method works. The key point here is to determine suitable values for $\kappa_{\max}$ and $\Delta\kappa$, which will be considered in section 5.1.2.

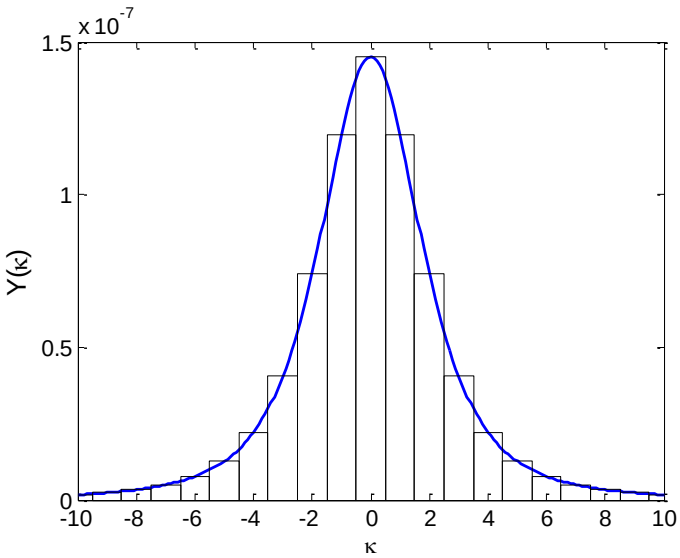

Figure 2.3. Integration in Eq. (2.4) is performed as a series of rectangles to approximate the area under the graph.

3. Wavenumber Boundary Element method for exterior problems

3.1 Fundamental solution

For time-harmonic linear acoustics, the Helmholtz equation may be used to describe the acoustic properties of the fluid system

$$\nabla^2\varphi(\mathbf{r})+k^2\varphi(\mathbf{r})=-\delta(\mathbf{r}-\mathbf{r_0}) \tag{3.1}$$

where $\nabla^2=\partial^2/\partial x^2+\partial^2/\partial y^2+\partial^2/\partial z^2$, φ is the fundamental solution at position $\mathbf{r}$, $-\delta(\mathbf{r}-\mathbf{r_0})$ is the three-dimensional Dirac delta function representing a source at any point $\mathbf{r}_0$ and $k=\omega/c$ is the acoustic wavenumber with c the acoustic wavenumber.

In free space, the solution of Eq. (3.1) is [11, 17, 18]

$$\varphi=\frac{e^{-ik|\mathbf{r}-\mathbf{r_0}|}}{4\pi|\mathbf{r}-\mathbf{r_0}|} \tag{3.2}$$

This function is also known as the free space Green's function for the pressure field due to a point source.

3.2 Boundary integral equation

Conceptually, to derive boundary integral equations, Green's second identity is applied to the two scalar functions p and φ. For exterior problems, a far-field boundary surface S_{R2} is introduced, along with the radiating surface S and the tiny spherical surface S_{R1} around the singular point, as shown in Figure 3.1. Therefore, Green's second identity becomes

$$\int_{V-V_{R1}}\left(\varphi\nabla^2 p-p\nabla^2\varphi\right)dV=\int_{S+S_{R1}+S_{R2}}\left(\varphi\frac{\partial p}{\partial n}-p\frac{\partial\varphi}{\partial n}\right)dS \tag{3.3}$$

where V is the acoustic domain exterior to S and V_{R1} is the tiny spherical volume.

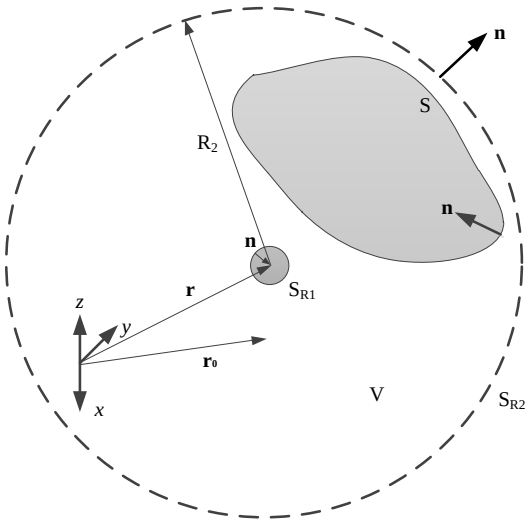

Figure 3.1. Illustration of the exterior problem (redrawn from [19])

Considering p is the sound pressure in the volume V and φ as defined in Eq. (3.2), it can be inferred that both functions satisfy Eq. (3.1). Hence the left-hand side in Eq. (3.3) is zero owing to cancellation of both the terms in V. For $\mathbf{r}$ in the acoustic domain, the integral over the tiny spherical surface is equal to $p(\mathbf{r}_0) \to p(\mathbf{r})$ as $R_1 \to 0$ while the integral over the far-field boundary in S_{R2} would vanish as $R_2 \to \infty$ due to Sommerfeld's radiation condition. It should be noted that the integral over the tiny spherical surface is dependent on position $\mathbf{r}$, e.g. for a smooth boundary it is equal to $1/2$ when $\mathbf{r}$ is at the boundary surface S. Therefore, in general, Eq. (3.3) reduces to

$$C(\mathbf{r})\, p(\mathbf{r}) = -\int_S \left(\varphi \frac{\partial p}{\partial n} - p \frac{\partial \varphi}{\partial n} \right) dS \tag{3.4}$$

where $C(\mathbf{r})$ is a coefficient dependent on position $\mathbf{r}$.

3.3 Wavenumber domain

Now the boundary variables, acoustic pressure p and fluid particle velocity in the direction $\mathbf{n}$, v_n, are conveniently expressed through the velocity potential ψ. This gives

$$v_n = -\frac{\partial \psi}{\partial \mathbf{n}} \tag{3.5}$$

and

$$p = \rho_0 \frac{\partial \psi}{\partial t} \tag{3.6}$$

where $\mathbf{n}$ is a unit direction vector and ρ_0 is the mean fluid density.

The WBE formulation of the fluid can be determined following Hamilton's principle

$$\left(\delta U - \delta T\right) - \delta W = 0 \tag{3.7}$$

where δU and δT are the first variation of the potential energy and the kinetic energy over a volume V respectively and δW is the virtual work at the boundary surface S. In terms of the velocity potential, the first variation terms in Eq. (3.7) in the frequency domain are defined as follows [9]

$$\delta U = \rho_0 \int_V k^2 \delta\psi^* \psi dV \tag{3.8}$$

$$\delta T = \rho_0 \int_V \nabla\left(\delta\psi\right)^{\mathbf{H}} \nabla\psi dV \tag{3.9}$$

$$\delta W = -\rho_0 \int_S \delta\psi^* \frac{\partial \psi}{\partial \mathbf{n}} dS \tag{3.10}$$

where $*$ denotes complex conjugate and $^{\mathbf{H}}$ is complex conjugate transpose.

Applying Green's second identity to the first variation of the kinetic energy in Eq. (3.9) gives

$$\rho_0 \int_V \nabla\left(\delta\psi\right)^{\mathbf{H}} \nabla\psi dV = \rho_0 \int_{S_A} \psi \frac{\partial \delta\psi^*}{\partial \mathbf{n}} dS - \rho_0 \int_V \delta\psi^* \nabla^2 \psi dV \tag{3.11}$$

where ∇^2 is the 3D Laplace operator. Substituting Eq. (3.8), (3.10) and (3.11) into Eq. (3.7) yields

$$\rho_0 \int_V \left(\delta\psi^* \nabla^2 \psi + k^2 \delta\psi^* \psi \right) dV + \rho_0 \int_{S_A} \left(\delta\psi^* \frac{\partial \psi}{\partial \mathbf{n}} - \psi \frac{\partial \delta\psi}{\partial \mathbf{n}} \right) dS = 0 \qquad (3.12)$$

where ∇^2 is the 3D Laplace operator.

Taking a spatial Fourier transform in the $x-$direction leads to the volume and surface integrals in Eq. (3.12) becoming surface and line integrals when the integral over wavenumber is dropped, hence

$$\rho_0 \int_S \delta\tilde{\psi}^* \left(\nabla_{2D}^2 \tilde{\psi} + \left(k^2 - \kappa^2 \right) \tilde{\psi} \right) dS + \rho_0 \int_\Gamma \left(\delta\tilde{\psi}^* \frac{\partial \tilde{\psi}}{\partial \mathbf{n}} - \tilde{\psi} \frac{\partial \delta\tilde{\psi}^*}{\partial \mathbf{n}} \right) d\Gamma = 0 \qquad (3.13)$$

where $\nabla_{2D}^2 = \partial^2/\partial y^2 + \partial^2/\partial z^2$, κ is the wavenumber in the $x-$direction, S is the cross-section area of the acoustic domain and Γ is the perimeter of the boundary. It can be seen that the first term of Eq. (3.13) is similar to the normal 2D Helmholtz equation but with k^2 replaced by $\alpha^2 = (k^2 - \kappa^2)$.

Now consider the presence of the point source. The first integral of Eq. (3.13) is required to be zero except at the source position. Meanwhile, following the derivation of the boundary integral in section 3.2, the second integral of this equation over the source constitutes $C(\mathbf{r})\delta\psi^*(\mathbf{r})$ where $|\mathbf{r} - \mathbf{r_0}| \to 0$. The integral over the far-field boundary also disappears owing to Sommerfeld's radiation condition. Hence, the boundary integral equation becomes

$$C(\mathbf{r})\delta\psi^*(\mathbf{r}) = -\int_\Gamma \left(\delta\tilde{\psi}^* \frac{\partial \tilde{\psi}}{\partial \mathbf{n}} - \tilde{\psi} \frac{\partial \delta\tilde{\psi}^*}{\partial \mathbf{n}} \right) d\Gamma \qquad (3.14)$$

The result from the BE model gives a relation between the boundary variables that may be written as

$$\mathbf{H}\tilde{\boldsymbol{\psi}} - \mathbf{G} \frac{\partial \tilde{\boldsymbol{\psi}}}{\partial \mathbf{n}} = \frac{\mathbf{P_{in}}}{i\omega} \qquad (3.15)$$

where $\tilde{\boldsymbol{\psi}}$ and $\partial\tilde{\boldsymbol{\psi}}/\partial\mathbf{n}$ are vectors of the respective variables at the nodes of the BE model and $\mathbf{n}$ is the unit vector normal to the surface of the boundary. To allow excitation by an incident wave field, $\mathbf{P_{in}}$ is introduced as the pressure amplitude of the incoming wave evaluated on the boundary nodes. $\mathbf{H}$ and $\mathbf{G}$ are generally full, non-

symmetric, complex-valued matrices that are obtained by discretising terms on the right-hand side of Eq. (3.14).

3.4 Mixed boundary condition

In addition to Eq. (3.15), another relation between the boundary pressure and the velocity is also required. This relation is given to cover specific conditions of the boundary, i.e. specifying a coupling to another system, for example nodes on the boundary which are not on the FE/BE interface (or 'wetted' surface). This is then referred to as a mixed boundary condition and can be written as

$$\mathbf{C}_A\tilde{\mathbf{P}} + \mathbf{C}_B\tilde{\mathbf{V}}_n = \mathbf{c}_c \tag{3.16}$$

where $\mathbf{C}_A$ and $\mathbf{C}_B$ are diagonal matrices and $\mathbf{c}_c$ is a vector corresponding to pressure sources and moving boundaries. Note that this boundary condition is also known as a Robin (or impedance) boundary condition. This kind of boundary condition is imposed in the present case to enforce zero velocity on the baffle and at the edges of the plate.

4. Coupling between WFE and WBE models

The work of the fluid on the structure needs to be taken account when they are coupled. Hence, the virtual work $\mathbf{C}_1\tilde{\mathbf{P}}$ produced by the WBE model can be included in the WFE model. This gives

$$\left(\mathbf{K}(\kappa) - \omega^2\mathbf{M}\right)\tilde{\mathbf{W}} - \mathbf{C}_1\tilde{\mathbf{P}} = \tilde{\mathbf{F}} \tag{4.1}$$

where $\mathbf{C}_1$ is a coupling matrix for pressure and $\tilde{\mathbf{F}}$ is an external force vector, if present.

At the wetted surface between the structure and the fluid, both models share the same nodes as well as having compatible shape functions. As a consequence of the essential boundary condition, the WFE and WBE models have the same normal velocity. In terms of the velocity potential, this can be expressed as

$$\mathbf{I}_2\frac{\partial\tilde{\boldsymbol{\psi}}}{\partial\mathbf{n}} - i\omega\mathbf{C}_2\tilde{\mathbf{W}} = 0 \tag{4.2}$$

where $\mathbf{I}_2$ is a matrix containing terms which are unity or zero and $\mathbf{C}_2$ is a transformation matrix transforming FE-displacements $\tilde{\mathbf{W}}$ to the equivalent normal displacement at the boundary.

From Eq. (4.2), $\partial\tilde{\boldsymbol{\psi}}/\partial\mathbf{n}$ can be written as

$$\frac{\partial\tilde{\boldsymbol{\psi}}}{\partial\mathbf{n}} = i\omega\mathbf{I}_2^{-1}\mathbf{C}_2\tilde{\mathbf{W}} \tag{4.3}$$

where the vector $\tilde{\mathbf{W}}(\kappa)$ is the displacement from the FE model. The velocity potential is obtained by substituting Eq. (4.3) into Eq. (3.15). This gives

$$\tilde{\boldsymbol{\psi}} = \mathbf{H}^{-1}\mathbf{G}\frac{\partial\tilde{\boldsymbol{\psi}}}{\partial\mathbf{n}} \tag{4.4}$$

Having obtained $\partial\tilde{\boldsymbol{\psi}}/\partial\mathbf{n}$ and $\tilde{\boldsymbol{\psi}}$, the particle velocity $\tilde{\mathbf{V}}_n(\kappa)$ and the pressure $\tilde{\mathbf{P}}(\kappa)$ and can be found from the Fourier transforms of Eq. (3.5) and (3.6).

Considering all relationships in Eq. (3.15)-(3.16) and Eq. (4.1)-(4.2) the combined system is obtained as follows

$$\begin{bmatrix} \mathbf{H} & -\mathbf{G}_n & \mathbf{0} \\ -i\omega\rho\mathbf{C}_1 & \mathbf{0} & \mathbf{K}(\kappa)-\omega^2\mathbf{M} \\ \mathbf{0} & \mathbf{I}_2 & -i\omega\mathbf{C}_2 \end{bmatrix} \begin{bmatrix} \tilde{\boldsymbol{\psi}} \\ \dfrac{\partial\tilde{\boldsymbol{\psi}}}{\partial\mathbf{n}} \\ \tilde{\mathbf{W}} \end{bmatrix} = \begin{bmatrix} \tilde{\mathbf{P}}_{\mathbf{in}} \\ \tilde{\mathbf{F}} \\ \mathbf{c}_c \end{bmatrix} \tag{4.5}$$

where $\mathbf{G}_n = \dfrac{1}{i\omega\rho}\mathbf{G}$.

4.1 Radiated sound power

The radiated power W_{rad} due to a vibrating waveguide structure is given by

$$W_{rad} = \frac{1}{2}\mathrm{Re}\left(\int_{-\infty}^{\infty}\int_{\Gamma} p(x)v_n^*(x)d\Gamma dx\right) \tag{4.6}$$

where Γ is the perimeter of the cross-section and $d\Gamma$ is an infinitesimal segment of the perimeter of the cross-section. By using Parseval's formula, Eq. (4.6) can be written in the wavenumber domain to give

$$W_{rad} = \frac{1}{4\pi}\mathrm{Re}\left(\int_{-k}^{k}\int_{\Gamma} \tilde{P}(\kappa)\tilde{V}_n^*(\kappa)d\Gamma d\kappa \right) \tag{4.7}$$

where the integral is restricted to $-k \le \kappa \le k$, with k the acoustic wavenumber, since elsewhere no radiated power is produced.

The integration process in Eq. (4.7) is actually performed element-by-element with the boundary variable $\tilde{P}_j$ and $\tilde{V}_j$ of each element j given by

$$\tilde{P}_j = \sum_{i=1}^{n} p_i N_i(\xi) \tag{4.8}$$

$$\tilde{V}_j = \sum_{i=1}^{n} V_i N_i(\xi) \tag{4.9}$$

where j is the element number, i is the node number of element j and $N_i(\xi)$ is the shape function with local coordinate $-1 \le \xi \le 1$.

The length of the infinitesimal segment itself can be evaluated by [11]

$$d\Gamma = \sqrt{(dy)^2 + (dz)^2} = \sqrt{\left(\frac{dy}{d\xi}\right)^2 + \left(\frac{dz}{d\xi}\right)^2}\, d\xi = J d\xi \tag{4.10}$$

where J is the Jacobian and

$$\frac{dy}{d\xi} = \sum_{i=1}^{n} y_i \frac{dN_i}{d\xi} \tag{4.11}$$

$$\frac{dz}{d\xi} = \sum_{i=1}^{n} z_i \frac{dN_i}{d\xi} \tag{4.12}$$

Therefore, the integration over the perimeter for each κ can be performed numerically. Here, standard Gaussian quadrature [20] is used for this. This gives

$$\begin{aligned}\int_{\Gamma}\tilde{P}\tilde{V}_n^{*}d\Gamma &= \sum_{j=1}^{m}\int_{\Gamma_j}\tilde{P}_j\tilde{V}_{n,j}^{*}d\Gamma \\ &= \sum_{j=1}^{m}\int_{-1}^{1}\sum_{i=1}^{n}p_iN_i(\xi)\left(\sum_{i=1}^{n}V_iN_i(\xi)\right)^{*}Jd\xi \\ &= \sum_{j=1}^{m}\sum_{k=1}^{g}w_k f(\xi_k)\end{aligned} \tag{4.13}$$

where m is the number of elements, g is the number of Gauss points used on the element, ξ_k is the k^{th} Gauss point, w_k is the corresponding weight and $f(\xi_k)=\sum_{i=1}^{n}p_iN_i(\xi)\left(\sum_{i=1}^{n}V_iN_i(\xi)\right)^{*}Jd\xi$.

4.2 Sound transmission

For an incident plane wave at angle θ to the normal (about the $x-$axis), the incident power per unit length in the $x-$direction is defined as

$$W_{inc}=\frac{1}{2}\int_{\Gamma}\frac{|p_i|^2\cos\theta}{\rho_0 c}d\Gamma \tag{4.14}$$

where $|p_i|$ is the incident pressure amplitude. The incident angle about the y - axis is determined by the wavenumber κ in the $x-$direction. By using the radiated sound power W_{rad} as defined by Eq. (4.7), the transmission coefficient is given by

$$\tau=\frac{W_{rad}}{W_{inc}} \tag{4.15}$$

The sound reduction index, or transmission loss, R is found from

$$R=10\log_{10}\left(\frac{1}{\tau}\right)\quad \text{dB} \tag{4.16}$$

In practice, structures are often subjected to a diffuse sound field rather than a plane wave. The diffuse sound field excitation is formulated as the superposition of uncorrelated plane waves with equal amplitude. The response of the structure is then

obtained by integrating the response due to all incident plane waves over the incident angle and weighting them with the corresponding solid angle to account for the directional distribution.

Using the same principle, the diffuse field can be defined in WANDS but a different convention is used owing to the way the acoustic response is calculated in WANDS. The acoustic response of the waveguide structure is calculated based on the wavenumber α instead of k as follows (see section 3)

$$\alpha = \sqrt{k^2 - \kappa^2} = \sqrt{k_y^2 + k_z^2} \tag{4.17}$$

The incident direction in WANDS can thus be described by two respective angles ϕ and β which cover the directional distribution of the acoustic intensity, as illustrated in Figure 4.1.

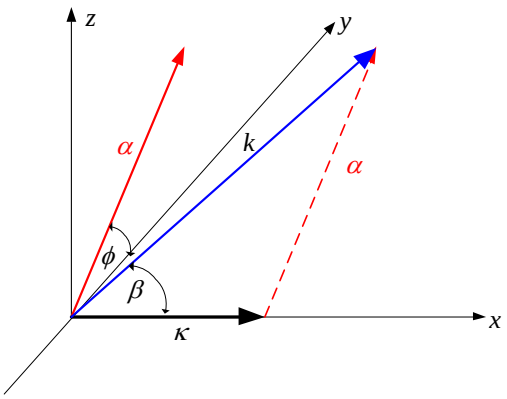

Figure 4.1. Description of incident direction in WANDS

Here ϕ is the angle within the $y-z$ plane (about the x axis) and β is the angle between the vectors of the acoustic wavenumber and propagating wavenumber in the x – direction (for $\phi = \pi/2$ it corresponds to a rotation about the y axis). Note that the angle β is dependent on κ while the angle ϕ is discretised from 0 to 90º.

As a consequence of the convention adopted in Figure 4.1, the wavenumbers in each direction can be defined as

$$k_x = \kappa = k \cos\beta \tag{4.18}$$

$$k_y = \alpha \cos\phi = \sqrt{k^2 - \kappa^2}\cos\phi = k \sin\beta \cos\phi \tag{4.19}$$

$$k_z = \alpha \sin\phi = \sqrt{k^2 - \kappa^2}\sin\phi = k \sin\beta \sin\phi \tag{4.20}$$

Following the Paris formula, the diffuse field transmission coefficients can thus be expressed as

$$\tau_d = \frac{\int_0^{\pi/2}\int_0^{\pi/2} \tau(\beta,\phi)\sin\beta\sin\phi d\Omega}{\int_0^{\pi/2}\int_0^{\pi/2} \sin\beta\sin\phi d\Omega} = \frac{4}{\pi}\int_0^{\pi/2}\int_0^{\pi/2} \tau(\beta,\phi)\sin\beta\sin\phi d\Omega \tag{4.21}$$

where $d\Omega = \sin\beta d\phi d\beta$. Hence, the sound reduction index or transmission loss for the diffuse sound field R_d is finally expressed by

$$R_d = 10\log_{10}\left(\frac{1}{\tau_d}\right) \quad \text{dB} \tag{4.22}$$

5. Validation case

A computer program has recently been developed at ISVR which implements the WFBE approach with a number of suitable element types [9]. This software package, called WANDS (Wave Number Domain Software), is used here to model the structure of a plate strip as well as the surrounding fluid for the case where the structure-fluid interaction exists. The detailed procedure for using WANDS is given in [8].

An aluminium plate of width $l_y = 1\,\text{m}$ and infinite length is assumed, with simply supported boundaries. The material and geometric properties are listed in Table 5.1.

Table 5.1. Material properties of the plate strip (unless otherwise stated).

Properties	Value
Young's modulus, E (N/m^2)	7.1×10^{10}
Poisson's ratio, ν_p	0.332
Thickness, h (mm)	6.0
Width, l_y (m)	1.0
Density, ρ (kg/m^3)	2.7×10^3
Damping loss factor (if used), η	0.1

5.1 Point mobility of a plate strip

In WANDS, a special element is implemented for plates consisting of a linear shape function for the in-plane motion and cubic Hermite polynomials for out-of plane motions. Here, unless otherwise stated, 30 plate elements are used to represent the cross-section of 1 m width. This corresponds to 4 elements per wavelength at the maximum frequency of 3 kHz. To simulate the simply supported boundaries, the first node of the first element and the second node of the last element are restrained in the x, y and z – directions but are free in rotation so that the model has 118 degrees of freedom (DOF) in total. A point force of unit amplitude is applied at the centre, which corresponds to the 16th node.

The WANDS software itself is used for calculating the matrices $\mathbf{K}_n$ and $\mathbf{M}$. Then, the receptance of the plate strip is obtained using the residue calculus method as described in section 2.5. The mobility of the plate strip is obtained by multiplying by $i\omega$. Figure 5.1 shows the point mobility of the plate strip along with the analytical result from [10]. It is clear that the numerical result agrees well with the analytical one for the parameters given.

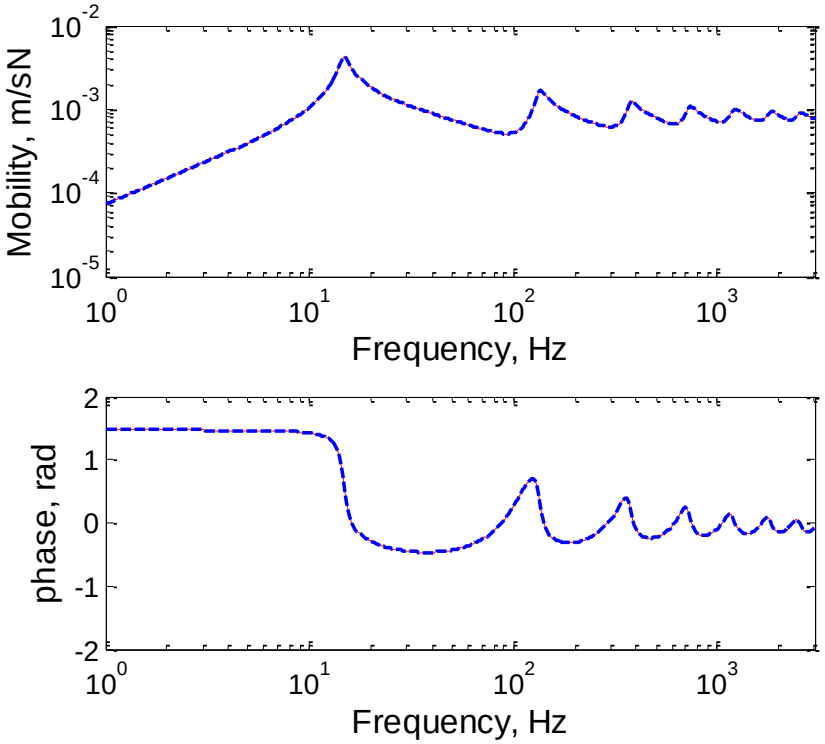

Figure 5.1. Mobility of the plate strip due to force excitation at $\left(0, l_y/2\right)$ calculated using WFE model (— numerical; --- analytical).

Figure 5.2 presents the predicted dispersion curves found from the free wave solutions for the undamped plate strip. Some mode shapes are also provided for particular cut-on frequencies. It is clear that the peaks found in the mobility are strongly related to the cut on of various waves.

In this figure, curves A and B are coupled longitudinal and shear waves resulting from in-plane displacement of the plate. These are not considered further in this report as this study is mainly devoted to the investigation of radiated power and sound transmission for lightweight structures. For these cases, the bending waves impose the largest normal displacement on contiguous fluid. Hence in terms of fluid-structure interaction, they are of most relevance.

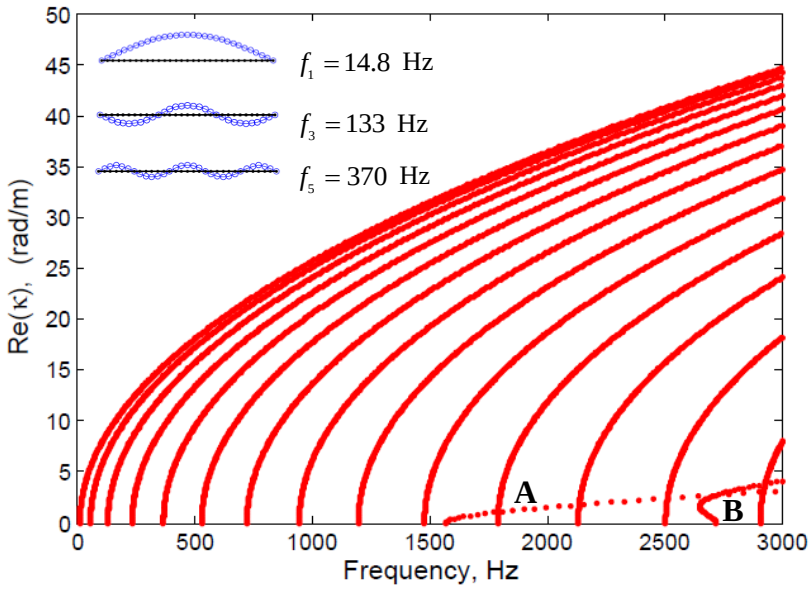

Figure 5.2. The predicted dispersion curves of a simply-supported plate strip and particular mode shapes.

Compared with the analytical results, the discrepancy in cut-on frequency is less than 1%, as shown in Table 5.2. This discrepancy increases with increasing frequency, indicating that the element density used in the model becomes less sufficient to cover the actual structural wavelength at these frequencies.

Table 5.2. Cut-on frequency f_m: comparison between numerical results and analytical ones.

m	f_m numerical	f_m analytical	% difference
1	14.8	14.8	0
2	59.2	59.2	0
3	133	133	0
4	237	237	0
5	370	370	0
6	533	533	0
7	725	725	0
8	947	947	0
9	1199	1198	0.08
10	1480	1479	0.07
11	1792	1790	0.10
12	2133	2130	0.14
13	2505	2500	0.20
14	2908	2899	0.30

5.1.1 Effect of element size

The required number of elements increases as frequency increases. As a rule of thumb, six finite elements or more are normally required per wavelength [21], although the element shape function also affects the accuracy. It has been seen that by including 30 elements in the model, the numerical result shows a good agreement with the analytical result up to 3 kHz. From Figure 5.2, it can be seen that at 1500 Hz 10 waves have cut on. The 10^{th} wave has 5 wavelengths across the width so that using 30 elements in the model gives 6 elements per wavelength at this frequency. By 3 kHz 14 waves have cut on and there are only 4 elements per wavelength.

Table 5.3 compares the results from WFE based on the residue calculus method with the analytical ones. Even at 3 kHz the agreement is within 0.3% in magnitude, as shown in Table 5.4. Reducing this to 10 elements, it can be seen that the results are much worse. This coarser mesh is sufficient up to 500 Hz where the error is less than 2% for the amplitude and 3 degrees for the phase. At this frequency it corresponds to 4 elements per wavelength. Hence, the results at higher frequencies are not strictly valid.

Table 5.3. Comparison of mobility calculated using analytical method and numerical method based on residue calculus.

Frequency (Hz)	Analytical		WFE Residue calculus			
	Magnitude ($ms^{-1}N$)	Phase (degrees)	Magnitude ($ms^{-1}N$)		Phase (degrees)	
			30 elements	10 elements	30 elements	10 elements
1	7.402×10^{-5}	84.27	7.402×10^{-5}	7.397×10^{-5}	84.27	84.27
10	1.052×10^{-3}	81.52	1.052×10^{-3}	1.052×10^{-3}	81.52	81.52
100	5.287×10^{-4}	15.73	5.287×10^{-4}	5.268×10^{-4}	15.73	15.19
500	7.842×10^{-4}	-12.83	7.844×10^{-4}	7.969×10^{-4}	-12.88	-15.11
1000	7.194×10^{-4}	-5.73	7.196×10^{-4}	7.430×10^{-4}	-5.87	-12.13
3000	7.645×10^{-4}	-4.87	7.666×10^{-4}	8.427×10^{-4}	-5.45	-19.17

Table 5.4. Relative error of numerical results compared with analytical results for certain frequencies.

Frequency (Hz)	Relative error			
	Magnitude (%)		Phase (degrees)	
	30 elements	10 elements	30 elements	10 elements
1	0	0	0	0
10	0	0	0	0
100	0	0.36	0	0.54
500	0.03	1.62	0.05	2.28
1000	0.03	3.25	0.14	6.40
3000	0.30	10.2	0.58	14.3

5.1.2 Effect of wavenumber range and step size on accuracy of mobility calculation

When the rectangle method is used, the calculation process experiences truncation in the wavenumber domain. In order to determine correct integration parameters, the results of this approach are compared with the residue calculus ones. They are used as the reference here as they include the same effects of discretization. The comparison is therefore limited to the effect of the integration method. Various wavenumber ranges and step sizes are considered. The maximum wavenumbers and step sizes are deliberately designed by considering them as multiples of the free bending wavenumbers k_B at the corresponding frequency, given by

$$k_B = \sqrt{\omega}\left(\frac{\rho h}{D}\right)^{1/4} \tag{5.1}$$

This approach allows a more general conclusion to be reached about how many wavenumbers should be included in the calculation. The error is obtained from comparison between the numerical results based on the rectangle method and the residue calculus one, defined as

$$\text{dB error} = 20\log_{10}\left|Y\right|_{\text{rectangle}} - 20\log_{10}\left|Y\right|_{\text{residue}} \tag{5.2}$$

The residue calculus results are given in Table 5.3. The wavenumber range and step size required to achieve an error less than 1 dB or 0.1 dB can be observed from Table 5.5. Note that the required maximum wavenumber and step size are compared to the real part of the free bending wavenumber at the corresponding frequency in order to get a non-dimensional maximum wavenumber and step size.

Some prominent features can be deduced from Table 5.5. Firstly, for low frequencies a high maximum wavenumber ratio is needed while a lower one is sufficient for mid and high frequencies. Secondly, a large step size ratio seems to be acceptable for low frequencies but as frequency increases a smaller step size ratio is required, particularly for mid frequencies. Thirdly, as expected, in order to achieve 0.1 dB error or less, a higher maximum wavenumber ratio and a smaller step size ratio are required than for 1 dB error. Therefore, the largest number of integration points is found in the mid frequencies for both error criteria.

This integration method has been considered as it is used by WANDS for the sound radiation and transmission. Other numerical integration methods such as Simpson's method should achieve a similar accuracy with less steps than the rectangle method [16]. However, the trend of the wavenumber range and step size required should follow the result of this study where the maximum wavenumber ratio decreases as frequency increases.

Table 5.5. Wavenumber ranges and step sizes required for 1 dB error and 0.1 dB error[1].

Frequency (Hz)	$\mathrm{Re}(k_B)$	1 dB error		0.1 dB error	
		$\frac{\kappa_{\max}}{\mathrm{Re}(k_B)}$	$\frac{\Delta\kappa}{\mathrm{Re}(k_B)}$	$\frac{\kappa_{\max}}{\mathrm{Re}(k_B)}$	$\frac{\Delta\kappa}{\mathrm{Re}(k_B)}$
1	0.816	≥ 5.5	≤ 2.75	≥ 18	≤ 2.25
10	2.579	≥ 1.5	≤ 0.75	≥ 4.5	≤ 0.375
100	8.156	≥ 1.25	≤ 0.1	≥ 3.75	≤ 0.12
500	18.24	≥ 1.0	≤ 0.05	≥ 2.0	≤ 0.03
1000	25.79	≥ 0.9	≤ 0.04	≥ 1.5	≤ 0.04
3000	44.67	≥ 0.9	≤ 0.04	≥ 1.5	≤ 0.02

[1] In practical calculation , the wavenumber range and step size is implemented:
$-(\kappa_{\max} - \Delta k/2) : \Delta k : (\kappa_{\max} - \Delta k/2)$

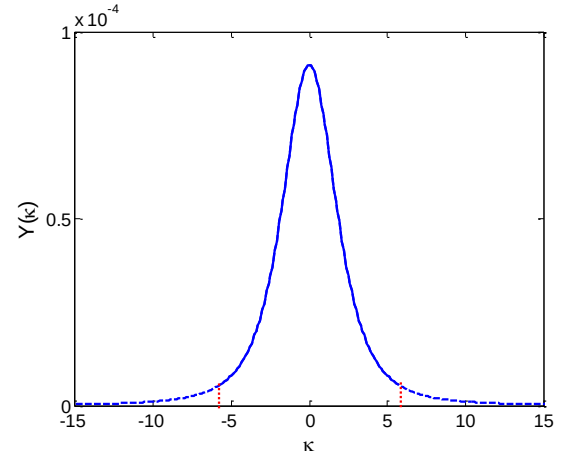

(a)

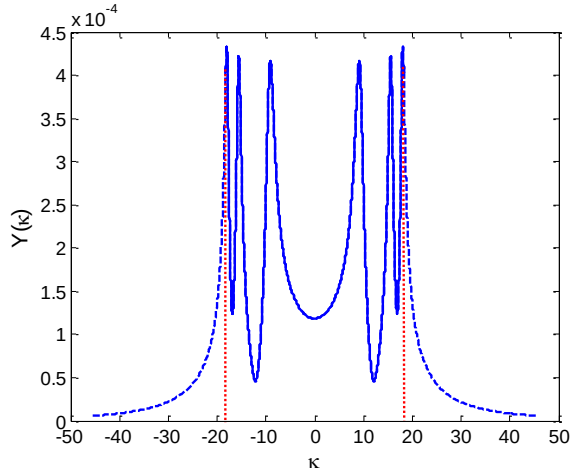

(b)

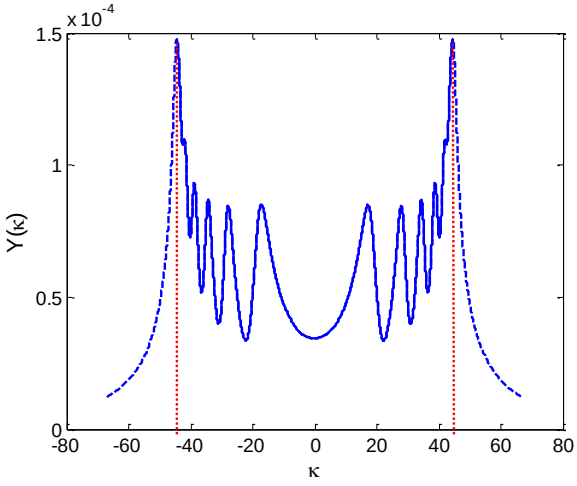

(c)

Figure 5.3. Mobility spectrum of the plate strip at (a) 1 Hz, (b) 500 Hz and (c) 3 kHz to represent low, mid and high frequencies respectively, with associated bending wavenumber of 0.8169, 18.27 and 44.74 rad/m (— range required for 1 dB error; - - - 0.1 dB error; • • • border for the region required for 1 dB error).

To clarify the effect of the wavenumber range included in the calculation, Figure 5.3 portrays the mobility spectrum in the wavenumber domain for three example frequencies based on Eq. (2.22) for $\eta = 0.1$. From this figure, it is clear that a wider range of wavenumbers relative to the bending wavenumbers is required at the low frequencies due to the presence of a single broad lobe. Therefore, the tail of the curve gives an important contribution to the total integral at low frequency. Meanwhile, for the mid and high frequencies a ratio of 1 is sufficient to cover most of the lobes and achieve an agreement within 1 dB. The tail of the spectrum should be included at these frequencies in order to achieve agreement within 0.1 dB. In terms of absolute step size, the mid frequencies need a smaller step size than at low and high frequencies because the peaks are quite close together and have a narrow bandwidth. It can be expected that for lower damping a smaller step size would be required.

5.2 Sound radiation of a plate strip

The radiated sound power has also been calculated using the coupled Wavenumber Finite Element-Wavedomain Boundary Element (WFBE) method. Figure 5.4 illustrates the WFBE model schematically. The WFE parameters are the same as for the WFE model used in the mobility calculation in section 5.1. To this is added a WBE model developed for an exterior problem using 30 cubic elements in all on the wetted surface. The first and last node of each element have the same coordinates as the WFE model as required in a coupled model, although the boundary elements have two intermediate nodes as well.

However, the analytical model used for comparison includes an infinite rigid baffle beyond the plate strip. In order to implement a rigid baffle in the numerical model, as will be shown this must comply with the following procedure: (i) the WBE sub-model should be included as an extended boundary element mesh on either side of the plate strip with a width of at least the acoustic wavelength under consideration; (ii) the WBE sub-model should be closed. The nodal surface velocity V_0 is set equal to zero for all nodes outside the wetted surface. For the current numerical model, a 1 m finite rigid baffle is included beyond both edges of the plate strip, unless otherwise stated, and this WBE mesh is 0.1 m thick. The effect of the size of this mesh is discussed in section 5.2.2. Note that the rear of the plate strip is not considered to radiate sound.

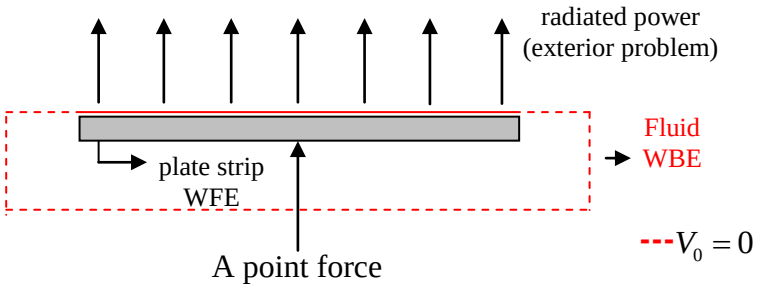

Figure 5.4. Schematic illustration of the plate strip excited by the acoustic plane wave.

The sound power radiation of the plate strip due to the point force excitation was calculated using Eq. (4.7). Figure 5.5 presents the radiated power for excitation at the centre (0, $l_y/2$) from the numerical and the analytical models. Some discrepancies can be observed from this figure, especially at low frequencies and around 2 kHz which corresponds to the critical frequency f_c. It is believed that the finite rigid baffle length of the numerical model affects the results in the low frequency region. This effect will be studied further in the next paragraphs. Meanwhile, the difference around f_c is believed to be due to difficulties in the implementation of the plate-fluid coupling in WANDS.

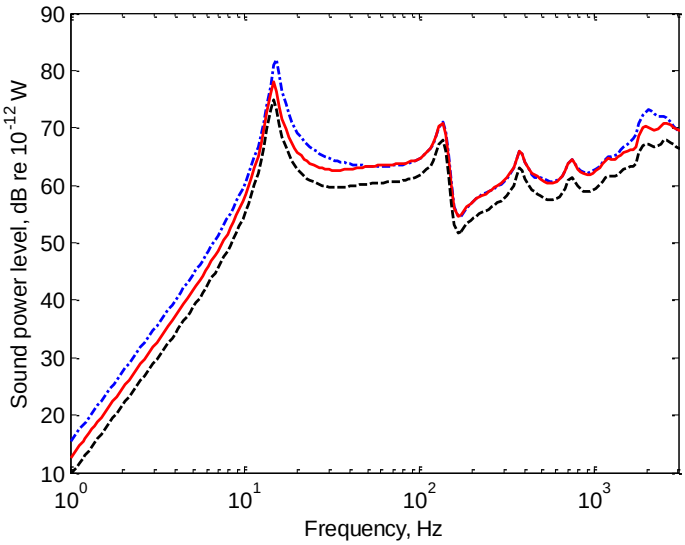

Figure 5.5 Comparison of the radiated power between numerical result and analytical one for excitation at the middle (0, $l_y/2$) (— numerical model; - - - numerical model with open BE mesh; – • – analytical model).

It can also be seen that a lower radiated power is obtained, where the result is not in agreement with that of the analytical model, when an open BE mesh is used.

This indicates that the inclusion of a closed BE mesh in numerical model is of importance to get a correct result.

5.2.1 Effect of baffle width

The analytical results are based on a plate strip set in an infinite baffle. In the WFBE results, this is approximated by a finite width baffle. The baffle width incorporated in the model affects the accuracy of the results, especially at low frequency. This is demonstrated here by varying the baffle width and then comparing the results with those of the analytical model. The baffle width is varied to be 0, 0.2, 1 and 2 metre extension from either edge of the plate strip. In other words, the length of the WBE sub-model on the radiating side for the 1 metre plate-strip will be 1.0, 1.4, 3.0 and 5.0 metre in total.

The results are shown in Figure 5.6. It is clear that the sound power level results from the numerical model become closer to the analytical ones when the baffle width increases. Thus a 1.4 m width baffle gives good agreement between the numerical results and the analytical ones at frequencies above 115 Hz while the agreement is extended down to 35 Hz for a 5 m width baffle. In contrast, the numerical model does not quite agree with the analytical one for any frequencies when the baffle is not present.

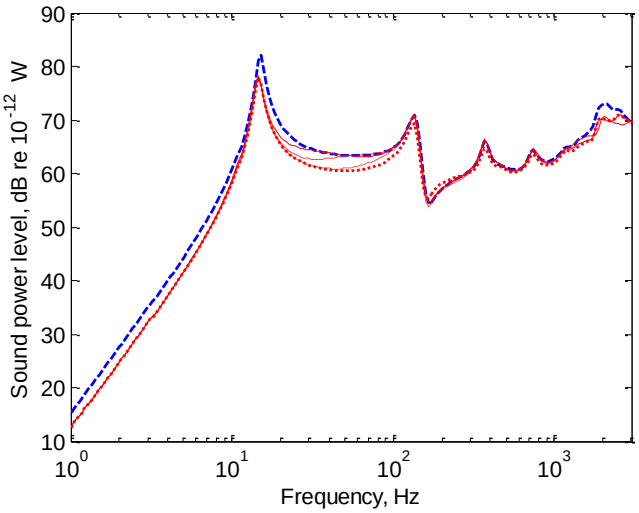

Figure 5.6. Radiated sound power calculated using the numerical model with various baffle width on each side of the plate and compared with those obtained with the analytical model (--- analytical model; — numerical model with baffle width of 2 m; --- baffle width of 1 m; – • – baffle width of 0.2 m; • • • no baffle exists)

These effects can be seen more clearly in Figure 5.7 which shows the level difference, defined as

$$\Delta W_{rad} = 10\log_{10}\left(\frac{W_{rad,numerical}}{W_{rad,analytical}}\right) \tag{5.3}$$

The value of ΔW_{rad} is approximately -3 dB at low frequency and reduces to 0 above a certain frequency. A large difference is found around at 15 Hz which is the first cut-on frequency. However, it should be noted that the fluid loading is neglected in the analytical model while this is considered in the numerical one. Hence, the difference greater than -3 dB at this frequency is caused by the fluid loading as well as the baffle width effect. Another large difference found at 2 kHz is related to the plate-fluid coupling issue at the critical frequency rather than the baffle width effect.

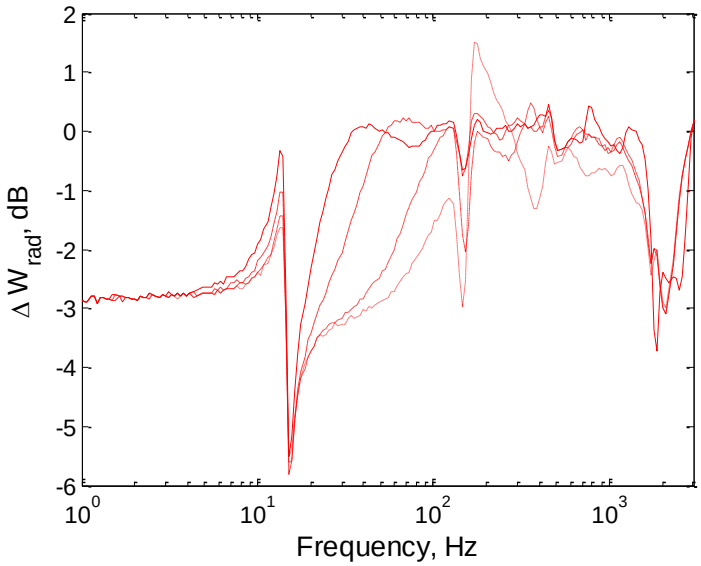

Figure 5.7. The baffle width effect on the radiated power in terms of radiated power differences relative to the analytical model (— baffle width beyond plate of 2 m; --- 1 m; – • – 0.2 m; ••• no baffle exists)

Considering these indications, it can be further concluded that the lowest frequency that can be covered by the model depends on the baffle width. The relation between the lowest frequency limit and the total width of the WBE mesh is summarized in Table 5.6. It can be seen that the lowest frequency limit reduces with

increasing baffle width. Therefore, the relation between the approximate lowest frequency of validity and the baffle width can then be shown to be

$$f_{ll} = \frac{c}{\lambda_{ll}} = \frac{c}{2l_b} \tag{5.4}$$

where f_{ll} is the lowest frequency limit and l_b is the total width of the WBE sub-model on the radiating side. Thus, in order to allow the numerical model to be used reliably down to 15 Hz for example l_b needs to be around 11 m. Accordingly, the 1 m wide structure would require a 5 m extension of the BE mesh beyond the structural width at both sides.

Table 5.6. Effect of baffle width on the lowest frequency limit for 1 m width structure

Baffle width (m)	Total width (m)	f_{ll} (Hz)
0.2	1.4	123
1.0	3.0	57
2.0	5.0	34

5.2.2 Effect of enclosed boundary thickness

Great care should be taken to avoid problems associated with thin bodies when developing the enclosed boundary element mesh. Otherwise, the Helmholtz integral equation in Eq. (3.14) becomes near-singular as the mesh of surface comes too close to that of the opposite surface (or line). Under such circumstances, the required jump in the double-layer potential is not generated as both surfaces collapse to the same surface so that the pressure is zero when the field point and source point are at the same surface. Moreover, the terms $\tilde{\psi}\left(\partial\delta\tilde{\psi}^*/\partial\mathbf{n}\right)$ of the Helmholtz integral equation is also zero as the normal velocities are equal and opposite on each surface. Consequently the presence of the singularity is never realized by the computer program so that the Boundary Element method produces unreliable results.

Specifically, this can be overcome by a thin-body integral formulation, e.g. as demonstrated in [11, 22]. In this study, however, the WBE model in WANDS is tested using different boundary thicknesses in order to avoid the problem. For this, four different enclosed boundary thicknesses are used to test the WBE model in WANDS. For the WBE thickness values of 6 mm, 15 mm, 30 mm, 66 mm and 100 mm are

selected. The effect of the boundary thickness is discussed in terms of the radiated power due to a point force.

Figure 5.8 shows the effect of thickness of the closed boundary WBE mesh. The results are identical for all thicknesses under consideration except for 6 mm where a 2 dB lower radiated power is found at low frequency. Therefore, the numerical model will produce good results if the thickness is 15 mm or more.

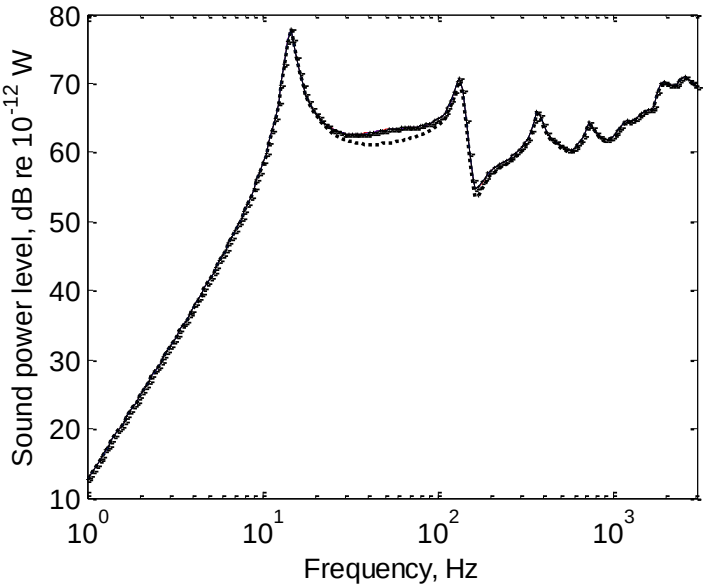

Figure 5.8. Effect of enclosed boundary mesh thickness (— 100 mm; --- 66 mm; – • – 30 mm; –+– 15 mm; ••• 6 mm).

5.3 Transmission loss of a plate strip

To calculate the transmission loss for the sound transmission problem, the numerical model is similar to that used for the radiated power calculations as discussed in section 5.2. The main difference exists in the form of excitation: in the transmission loss case, a plane acoustic wave is used instead of the point force, as shown in Figure 5.9. The numerical model is developed using a coupled WFBE model consisting of one WFE region representing the plate strip structure and two WBE-fluid regions for modelling the sound pressure field on both sides of the structure. The wavenumbers of the plane waves are governed by the incidence angle, which depends on the elevation and azimuthal angles for a 3-D problem. Moreover, 50 cubic plate elements are now used to cover the 1 m width in order to extend the result to a higher frequency. Under such circumstances, the model is expected to be

acceptable up to 8.5 kHz at which it corresponds to 4 elements per structural wavelength. However, it is important to compare the model configuration with the acoustic wavelength as the structural wavelength is larger than this above the critical frequency of 2.0 kHz. In fact, compared with the acoustic wavelength there are only 2 elements per wavelength. Nevertheless, this number of elements is still sufficient due to the cubic shape function.

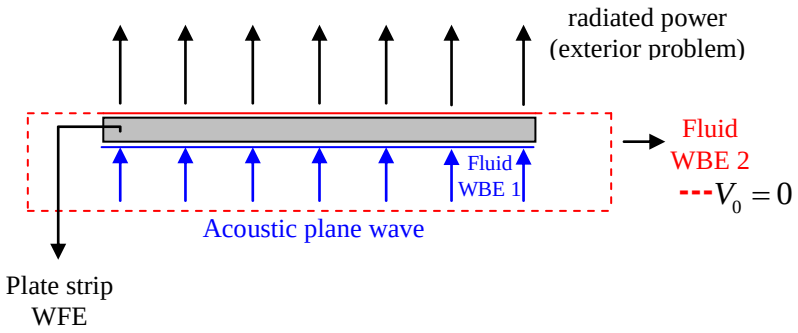

Figure 5.9. Schematic illustration of the plate strip excited by the acoustic plane wave.

For simplicity, the model differs from the WBE model of the radiation problem as the incoming plane waves are realized by an open boundary mesh. This causes differences in the scattered field on the source side. In order to assess the effect of the open boundary mesh, the result obtained is compared with that of the closed boundary one using the following formula:

$$\Delta STL = 10\log_{10}\left(\frac{\tau_{\text{closed boundary}}}{\tau_{\text{open boundary}}}\right), \qquad \text{dB} \qquad (5.5)$$

The result is presented in Figure 5.10. It is clear that the highest difference occurs at the first cut-on frequency, 14.8 Hz, at which a difference of 2.5 dB is found. As the frequency increases, the level difference reduces and it is less than 0.5 dB for frequencies above 40 Hz. This behaviour is caused by fluid loading at low frequencies which becomes negligible at higher frequencies. Hence the open boundary used in this study will not affect the accuracy of the numerical results for the current case for frequencies above 63 Hz as usually considered in practice.

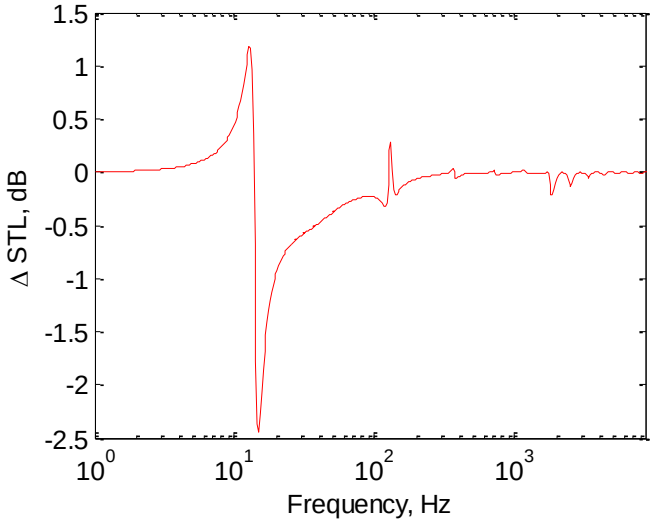

Figure 5.10. The difference in the transmission loss between open boundary and closed boundary mesh on the source side.

5.3.1 Normal incidence case

Figure 5.11 presents a comparison between the numerical result and the analytical one for normal incidence. Note that the analytical model for this case has been extended from that given in [10] by including the cross-terms between different mode orders. The modified formulation is given in Appendix A. The mass-law result is also shown for comparison.

First of all, the trend of the transmission loss in the numerical results agrees well with the analytical one. For the case under consideration, the transmission loss follows the mass law trend as frequency increases, especially above 100 Hz. Below 50 Hz, a discrepancy occurs due to the finite baffle width (see section 5.2.1); hence it will always appear below some frequency depending on the assumed baffle width considered in the numerical model. Apart from this, the numerical result agrees well with the analytical one. Various peaks and dips are seen corresponding to cut-on frequencies of odd modes. The even modes are not excited in this case of normal incidence.

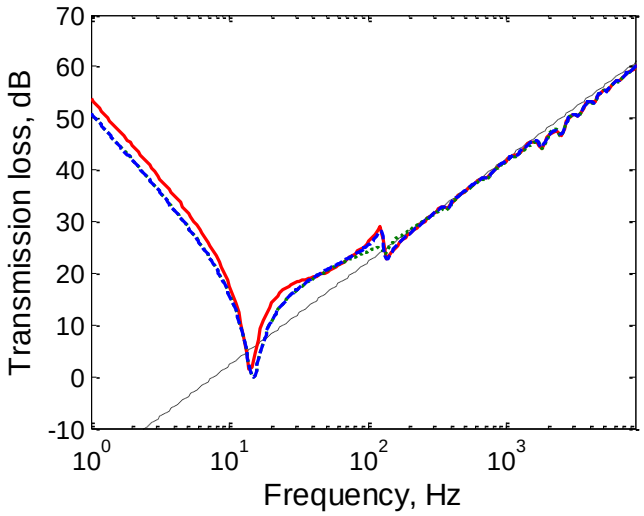

Figure 5.11. Comparison of transmission loss of the plate strip based on the numerical model and the analytical one (— numerical model; --- analytical model; ••• analytical model without cross-term contribution; – • – mass law).

It can be also seen that the results of the analytical model with and without including the cross-term contribution in the calculation are very similar except between 80 and 200 Hz. Hence, for this case, the model without the cross-term contribution can be considered to achieve a sufficient accuracy, except in this frequency region, without requiring a high computational time.

5.3.2 Oblique incidence case

A further comparison can be carried out for an oblique incidence angle. The plate strip is subject to a plane wave impinging on it at a certain angle to the normal. For the plate strip case, it is possible to construct the incident angle about the x axis or y axis, where each of them would affect the transmission loss behaviour differently due to the nature of the plate strip dimension. Figure 5.12(a) shows the result for oblique incidence at an angle of 45º about the $x-$axis and Figure 5.12(b) is the result for the same elevation angle but about the $y-$axis. Both cases show a good agreement with the analytical result, with the dips in the curves corresponding to the cut-on frequency behaviour. Due to the finite width of the plate strip, the modal behaviour is more pronounced for the former case, where even modes as well as odd modes are excited, than it is for the latter one.

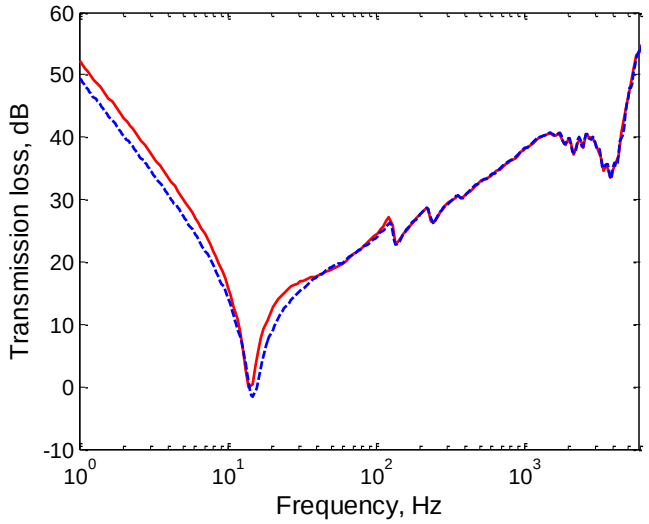

(a)

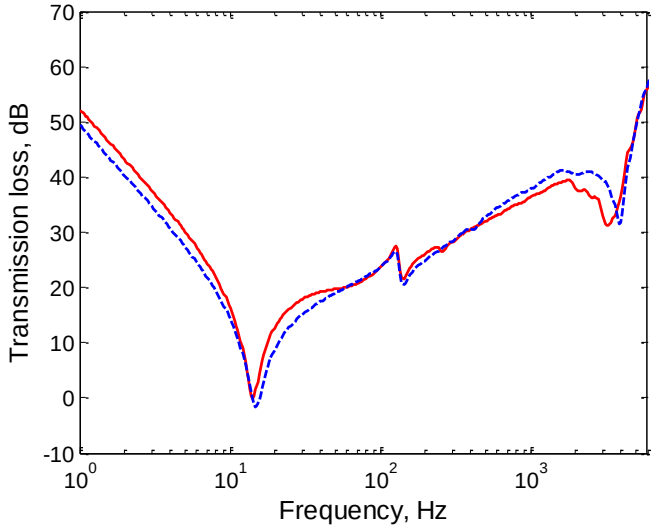

(b)

Figure 5.12. Comparison of transmission loss of the plate strip and the analytical model for oblique incidence case: (a) $\theta = 45^\circ$; $\varphi = 90^\circ$ (b) $\theta = 45^\circ$; $\varphi = 0^\circ$ (— numerical model; --- analytical model).

Above the critical frequency, the coincidence frequency calculated by the numerical model agrees with that of the analytical model for the former case. However, it is slightly lower than the analytical one for the latter case. This unmatched coincidence frequency would lead to an erroneous result for the diffuse sound field in which the plane waves from all incident angles are evaluated in the transmission loss calculation. This discrepancy is believed to be related to the errors found in the sound radiation result around the critical frequency (see Figure 5.5).

Moreover, it has been found (not shown here) that the error increases as the incidence angle is increased.

5.3.3 Effect of plate thickness

Figure 5.13 shows results for two different plate thicknesses, 6 mm and 9 mm, for normal incidence. The numerical results show a good agreement with the analytical ones. The increasing transmission loss is expected and the dip related to the first cut-on frequency shifts upward with increasing thickness.

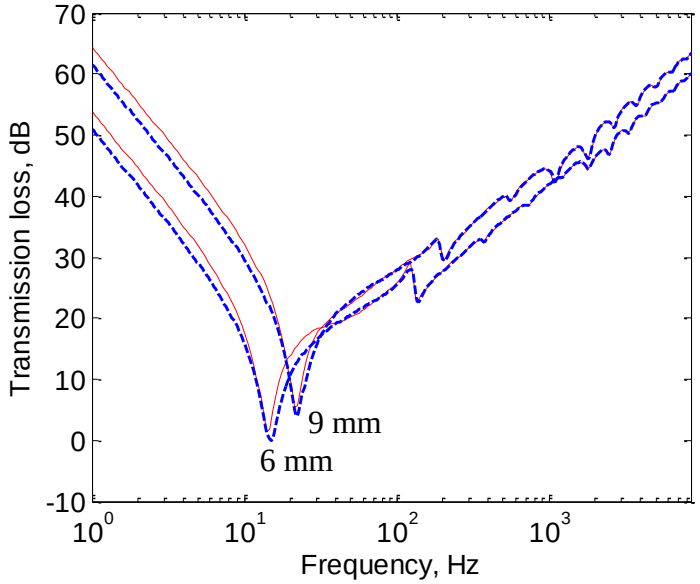

Figure 5.13 Comparison of transmission loss of the plate strip based on the numerical model and analytical model for the case of the different thickness (— numerical model; --- analytical model).

5.3.4 Effect of damping loss factor

Figure 5.14 shows results for a smaller damping loss factor η of 0.01, again for normal incidence. A good agreement is found with the analytical model, with dips in the transmission loss at the various (odd) cut-on frequencies.

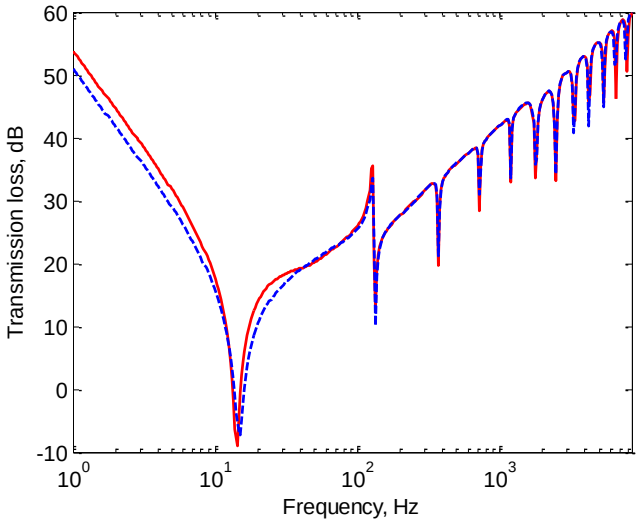

Figure 5.14. Comparison of transmission loss of the plate strip and the analytical model for lower damping loss factor $\eta = 0.01$ (— numerical model; --- analytical model).

5.3.5 Diffuse sound field

In the previous analysis, the resulting transmission loss was calculated for excitation by an acoustic plane wave. Now the structures are subjected to a diffuse sound field excitation and the sound pressure level is calculated using the procedure in section 4.2. For this, 9 incident angles ϕ about the x axis and 18 incidence angles β are considered with an upper angle of 90º. Figure 5.15 presents a comparison of transmission loss from the numerical model and analytical one under a diffuse sound field excitation. The results of the numerical model are in a good agreement except around and above the critical frequency. Around the critical frequency, the WFBE model has a higher transmission loss than the analytical one while the dip associated with the critical frequency occurs at 2179 Hz for the numerical model instead of 2034 Hz as shown by that of the analytical model. Moreover, above this frequency the transmission loss of the plate element model starts to deviate and has lower values than the analytical results. Therefore, it is clear that the numerical model gives erroneous results in this frequency region.

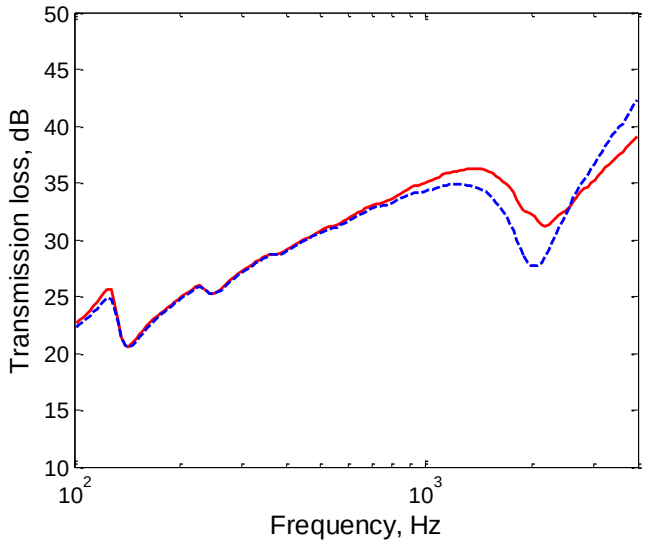

Figure 5.15. Transmission loss comparison of the numerical models and the analytical model under a diffuse sound field excitation (— numerical model using plate elements; --- analytical model).

6. Substitution of plate elements by solid elements

All cases considered in the previous sections will now be repeated using a model assembled using solid finite elements instead of plate elements. The results obtained will be compared with those of the plate elements and the analytical model. All procedures and formulae used for the plate element case are again used for calculating the results with the solid elements, hence the description of that is not repeated in this section. Furthermore, the material properties are the same as used for the plate element model (see Table 5.1).

To realize the WFE model using solid elements, eight-noded quadrilateral elements are used with quadratic polynomial shape functions. Three-noded boundary elements are used for WBE fluid with 1 metre extension on both sides beyond the length of the plate strip in order to represent the rigid baffle. Hence the width of the BE mesh at the radiation side is 3 m in total. The elements at the edges are restrained in three directions at their mid-side points to impose simply supported boundary conditions, as shown in Figure 6.1. The effect of restraining the nodes is considered in detail in section 6.2.

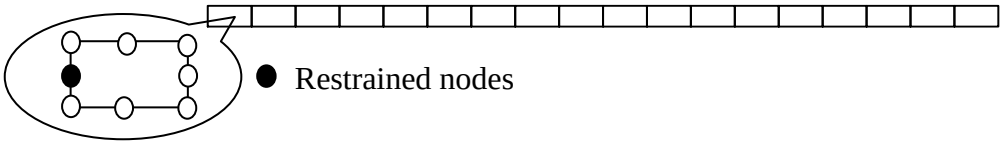

Figure 6.1. Restrained node for simply supported boundary conditions in the solid element model.

6.1 Element density

The element density used for the plate elements, which is 30 elements for 1 m width plate strip, is not sufficient to produce the same results up to 3 kHz for the case of the solid elements. After increasing the density up to 50 elements, the dispersion curves of this model become closer to those of the plate element model, as shown in Figure 6.2. This indicates that it requires seven elements per wavelength if the quadrilateral type of solid element is used while four elements per wavelength are sufficient for the case of the plate elements. This element density gives 0.3% difference in frequency relative to the plate element result and 0.6% compared with the analytical results at around 2.9 kHz (which is the 14th cut-on frequency). Hereafter, this element density is implemented for all comparisons considered except for particular cases where a higher maximum frequency is required.

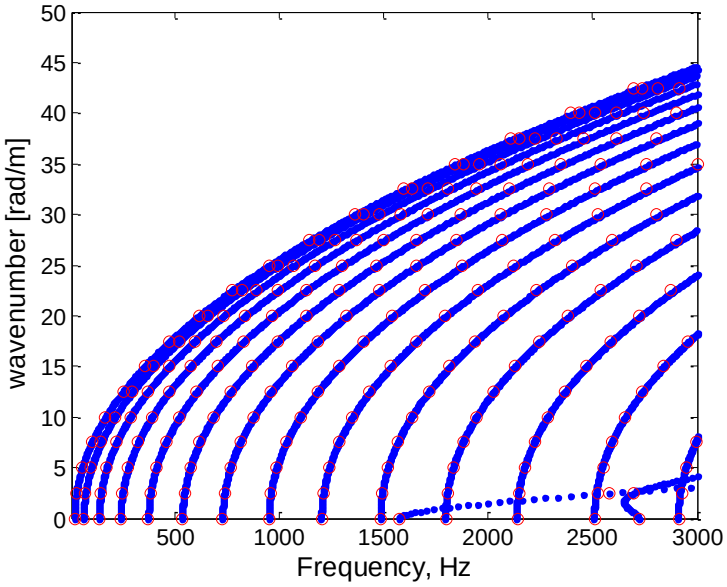

Figure 6.2. Dispersion curve comparison of the plate element model and the solid element one (● Plate element ; ○ solid element)

6.2 Effect of restrained nodes

Restrained nodes are of importance in realizing certain boundary conditions in the numerical model. In order to see the effect on the boundary conditions, three different configurations of restrained nodes of the solid elements are considered. This can be seen from Figure 6.3 where only a corner node is restrained in configuration (a), a midside node for configuration (b) and combination of both the corner and midside node for the configuration (c). In each case all three translations are restrained; unlike plate elements, solid elements do not have rotational degrees of freedom.

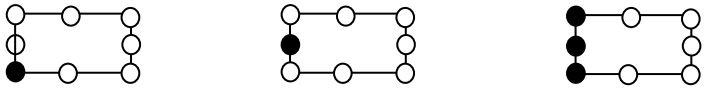

Figure 6.3. Restrained nodes position of an solid element (● restrained node)

The effect of the restrained node position is compared in terms of dispersion characteristics in Figure 6.4 and the cut-on frequencies corresponding with each configuration are listed in Table 6.1. Considering the relationship of the cut-on frequencies and the boundary conditions, it can be inferred that the cut-on frequencies of configuration (b) correspond to the simply supported boundary conditions. The corresponding analytical results are $\left(m\pi/l_y\right)^2\left(D/\rho h\right)^{1/2}$ with l_y the panel width, D bending stiffness, ρ structural density and h structural thickness. Meanwhile, configuration (c) can be inferred to correspond to the clamped boundary condition in which the cut-on frequencies equal approximately $\left[\left(m+1/2\right)\pi/l_y\right]^2\left(D/\rho h\right)^{1/2}$. For configuration (a) the results are affected by coupling with the longitudinal waves due to the asymmetrical constraint.

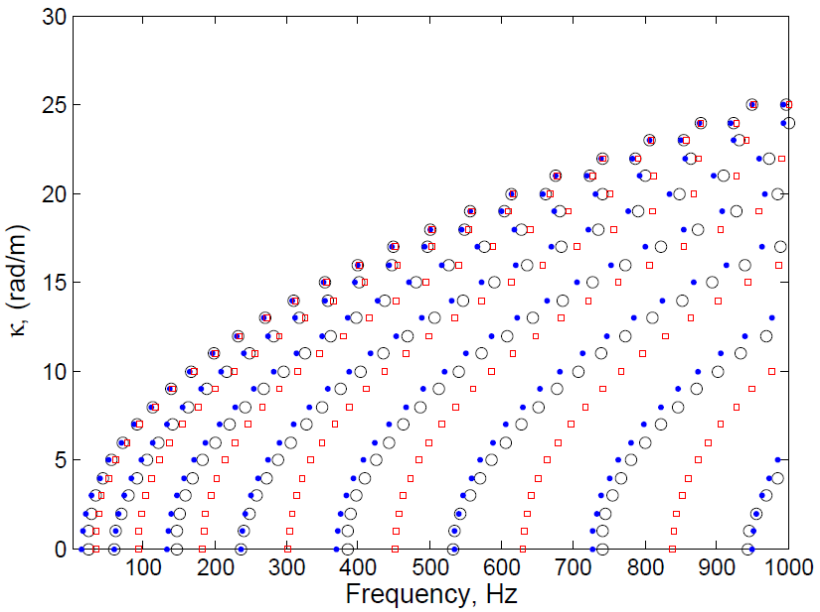

Figure 6.4 Dispersion curve comparison of configurations in Figure 6.3 (○ configuration (a); ● configuration (b) ; □ configuration (c)).

Table 6.1. Cut-on frequencies f_m corresponding with configurations in Figure 6.3.

	f_m (Hz)				
m	Numerical			Theoretical	
	(a)	(b)	(c)	Simply supported	Clamped
1	23.6	14.8	33.3	14.8	33.3
2	59.3	59.2	92.4	59.2	92.4
3	146.5	133	181	133	181
4	237	237	302	237	300

6.3 Point mobility

A point force is applied at the centre of the plate strip at position $\left(0, l_y/2\right)$. In terms of amplitude, the mobility of the solid element model is in good agreement with that obtained by the plate element model as well as the analytical model, as shown in Figure 6.5. However, the differences are found to be greater at high frequencies; e.g. at 3 kHz it is found that the mobility amplitude of the solid model is 0.4% higher than the plate element model while its phase is 0.12 radian higher than the plate element model. Compared with the analytical model, differences of 0.7% for the amplitude and of 0.13 radian for the phase are found.

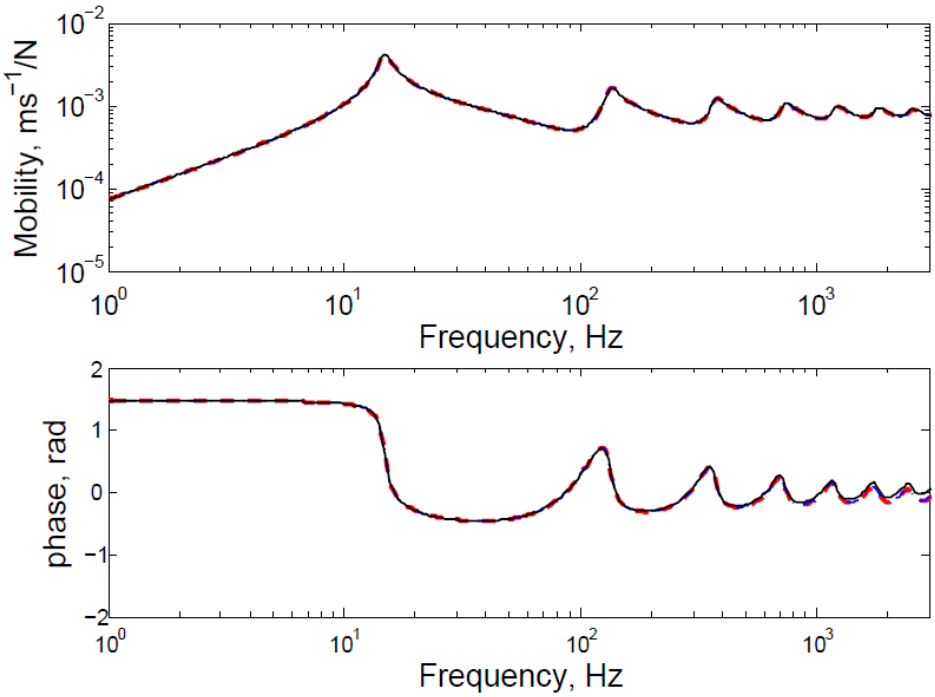

Figure 6.5. Mobility comparison of the solid element model and the plate element model (— solid element; --- plate element; —•— analytical model).

6.4 Radiated sound power

It has been shown in section 5.2 that the plate element model result has a discrepancy in the radiated sound power around the critical frequency f_c. To re-evaluate the numerical model for this frequency region, the analytical results are also included along with the plate element model result. The comparison of these results for radiated sound power can be seen in Figure 6.6. It is clear that the solid element model produces a better result for the frequency range of interest, particularly around f_c, when the results are compared with those of the analytical model. At low frequency, both the numerical models produce around 3 dB lower radiated power than the analytical model as a consequence of the baffle width included in the models (see section 5.2.1).

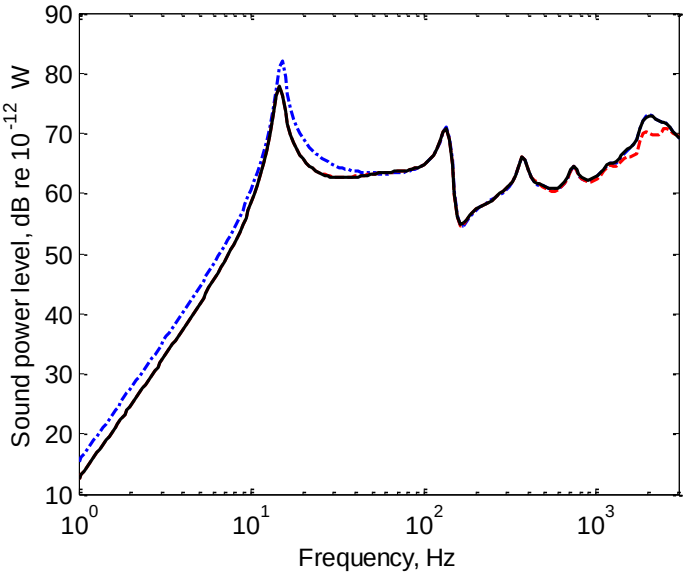

Figure 6.6. Radiated power comparison (— solid element; --- plate element; —•— analytical model)

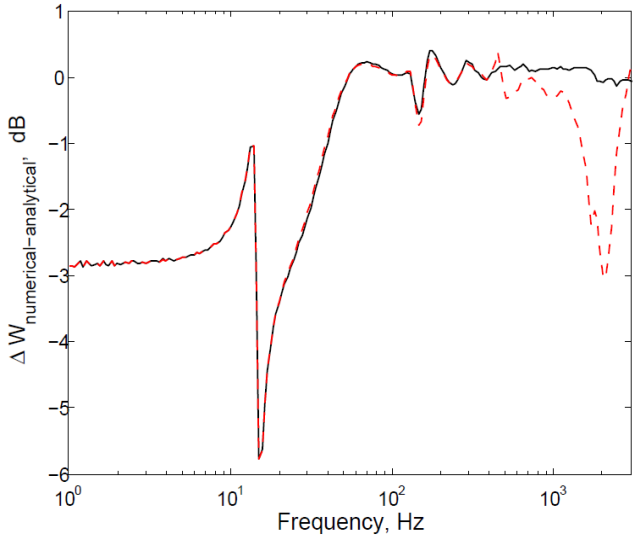

Figure 6.7. Radiated power level difference between the numerical model and the analytical one (— solid element model and analytical; --- plate element model and analytical).

Figure 6.7 presents the level difference of the radiated power between both the numerical models and the analytical one. It is clear that around the critical frequency a difference of up to 3 dB exists for the plate element model whereas the solid element model shows a difference of less than 0.2 dB in this frequency region. Apart from this frequency region, the difference between the numerical models and the analytical one at low frequencies is clearly due to the baffle width effect as found previously.

6.5 Transmission loss

To cover a higher frequency range up to 6 kHz, which is considered to be sufficient for oblique incidence with angle of 45°, the number of elements is increased to 70 elements covering 1 m width plate strip. At this frequency, there are 7 elements per structural wavelength and 4 elements per acoustic wavelength. Figure 6.8 presents a comparison of the transmission loss for the solid element model, the plate element and the analytical one for the normal incidence case. At frequencies above 50 Hz, the results of the solid element model agree well with those of the plate element model and the analytical one. Meanwhile, the solid element model results agree with the plate element ones for all frequencies.

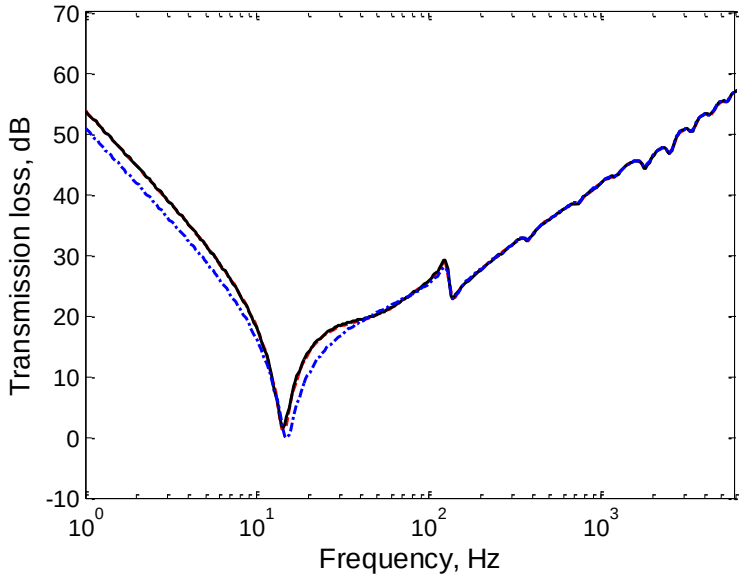

Figure 6.8. Transmission loss comparison of the model with solid element and plate element for normal incidence case (— solid element; --- plate element; —•— analytical model).

For the case of oblique incidence at an angle about the x axis, the results are shown in Figure 6.9(a). The solid element model generally produces promising results compared with the plate element model and the analytical one below the coincidence frequency. Above this frequency, the transmission loss of the solid element model starts to deviate slightly from the plate element model and the analytical results. This indicates that the solid element model requires a higher element density to cover this frequency region. For the case of an incident angle about the y axis, as shown in

Figure 6.9(b), it is clear that the solid element model results agree well with the analytical results whereas the plate element model results differ considerably below the coincidence frequency and at the coincidence frequency itself.

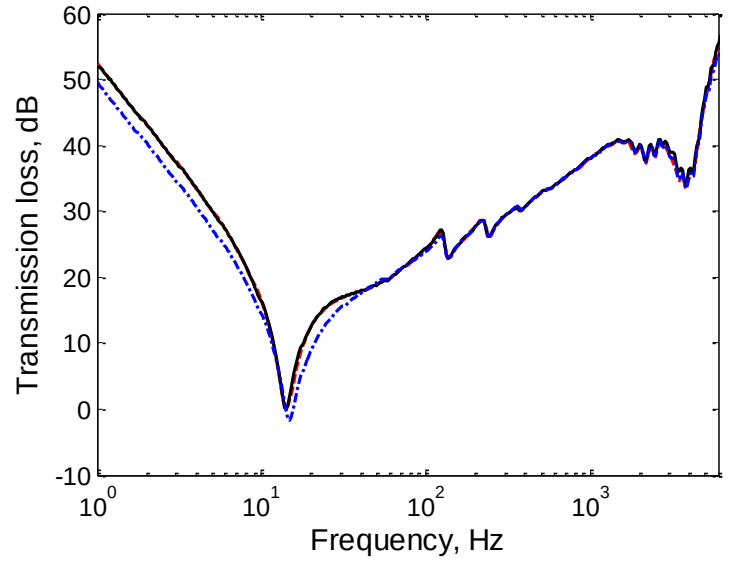

(a)

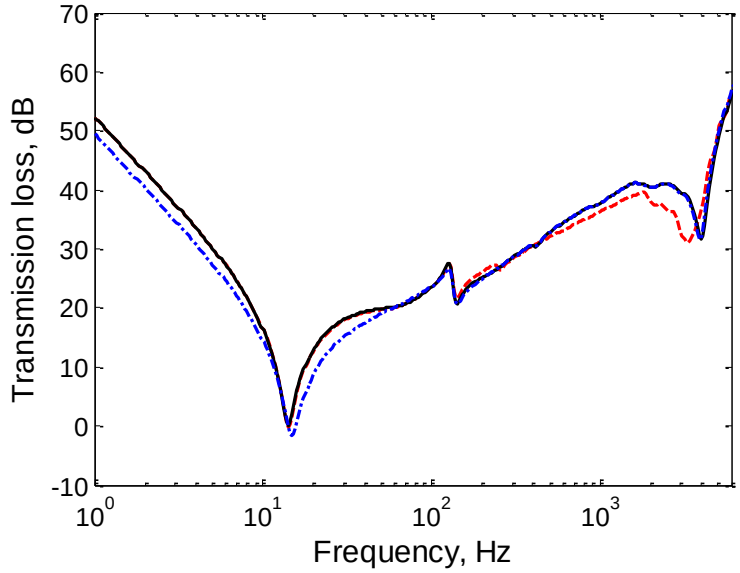

(b)

Figure 6.9. Transmission loss comparison of the model with solid element and plate element for oblique incidence case: (a) at angle 45º about x axis; (b) at angle 45º about y axis (— solid element; - - - plate element; —•— analytical model).

6.6 Diffuse sound field

As in section 5.3.5, the diffuse sound field is represented by an integral over a range of incident angles with an upper angle of 90° to represent full random incidence; hence the upper angle 90º is chosen here. These results are shown in Figure 6.10. From this, it can be seen that the solid element model gives results that are much closer to the analytical ones than the plate element model, particularly around and above the critical frequency. Such trends have already been observed in Figure 6.9.

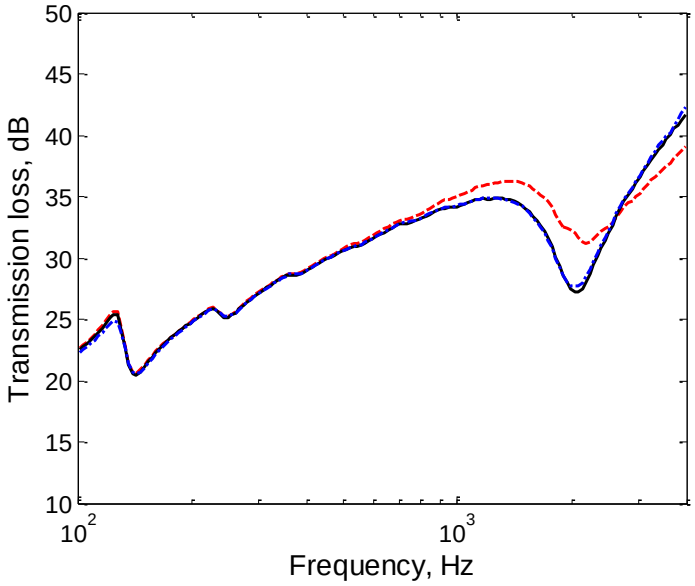

Figure 6.10. Transmission loss comparison of the numerical models and the analytical model under a diffuse sound field excitation (— solid element; --- plate element; – • – analytical model).

7. Summary

Comparisons of numerical results and analytical ones have been conducted to validate the WFBE method applied in this study and to determine under what circumstances the numerical model can be used to give accurate results. For the mobility calculation a suitable wavenumber range and step size are determined in order to ensure errors are less than a certain value. This range is expressed in terms of the maximum wavenumber ratio, relative to the associated free bending wavenumber of the plate. This study shows that the maximum wavenumber ratio decreases as frequency increases e.g. for the case considered at 1 Hz $\kappa_{\max}/\mathrm{Re}(k_B) = 18$ while $\kappa_{\max}/\mathrm{Re}(k_B) = 1.5$ for 3 kHz in order to get results with an error of less than 0.1 dB.

Some practical aspects of implementing this method using the WANDS software should be borne in mind in order to obtain correct results. Firstly, the Waveguide Boundary Element (WBE) domain should have a closed boundary. The thickness of the mesh should be determined carefully to avoid the jump phenomenon which causes misleading results. Secondly, to simulate a baffled situation a finite rigid baffle should be included in the model by extending the width of the WBE fluid model beyond the structure. The width of the finite rigid baffle is important in determining the accuracy of the numerical model results at low frequency in comparison with the analytical ones which are for an infinite baffle. The lowest frequency at which the numerical model results are still valid depends on the total width of the baffle at the radiating side which should be at least half the acoustic wavelength. Thirdly, care should be taken in choosing the element type in the WANDS software. For the case of the waveguide structure considered in this study, the plate element type along with its coupling element to acoustic BE fails to calculate accurately the vibro-acoustic response of the plate strip although it gives good results for the mobility. It is found that the radiated sound power is incorrect in the critical frequency region and the transmission loss is incorrect around and above the coincidence frequency. To overcome this, solid elements can be used to obtain the results although a higher element density is required to achieve the same level of precision.

All in all, the WFBE method is applicable for the cases considered in this study. Moreover, the WANDS software can be used to develop numerical models of

structures and the structure-fluid interaction provided that suitable precautions are taken.

8. Recommendations for future work

Problems associated with the implementation of the numerical model require further attention in the WANDS software. The following work is recommended to be considered for such a purpose in future:

1. It is required to have analytical models of simple cases to validate the results of WANDS. It is particularly useful for testing the cases incorporating coupling models, e.g. plate-fluid coupling model, before proceeding to handle multi-domain models in which more than two sub-models are used. The results obtained can then be used to update WANDS if discrepancies are found.
2. To extend the capability of WANDS in modelling various multi-domain systems, the WANDS software should be able to handle and process complex wavenumbers as input.
3. It is also important to have a better documentation of the source code of WANDS to allow computational errors to be traced more easily as well as assisting the incorporation of new sub-model into the WANDS software in the future.

9. References

1. Nilsson, C.-M., *Waveguide Finite Elements Applied on a Car Tyre*. 2004, MWL KTH: Stockholm.
2. Nilsson, C.M., et al., *A waveguide finite element and boundary element approach to calculating the sound radiated by railway and tram rails.* Journal of Sound and Vibration, 2009. **321**(3-5): p. 813-836.
3. Nilsson, C.-M., et al. *A coupled waveguide finite and boundary element for calculating the sound transmission through complex panel structure*. in *IX International Conference on Recent Advances in Structural Dynamics*. 2006. University of Southampton UK.
4. Bartoli, I., et al., *Modeling wave propagation in damped waveguides of arbitrary cross-section.* Journal of Sound and Vibration, 2006. **295**(3-5): p. 685-707.
5. Gavric, L., *Computation of propagative waves in free rail using a finite element technique.* Journal of Sound and Vibration, 1995. **185**(3): p. 531-543.
6. Finnveden, S., *Spectral finite element analysis of the vibration of straight fluid-filled pipes with flanges.* Journal of Sound and Vibration, 1997. **199**(1): p. 125-154.
7. Waki, Y., B.R. Mace, and M.J. Brennan, *Free and forced vibrations of a tyre using a wave/finite element approach.* Journal of Sound and Vibration, 2009. **323**(3-5): p. 737-756.
8. Nilsson, C.-M. and C.J.C. Jones, *Manual for WANDS 2.1, ISVR technical memorandum No.976*. 2007, University of Southampton: UK.
9. Nilsson, C.-M. and C.J.C. Jones, *Theory manual for WANDS 2.1, ISVR technical memorandum No.975*. 2007, University of Southampton: UK.
10. Prasetiyo, I. and D.J. Thompson, *Vibration response, sound radiation and sound transmission of an infinite plate strip*, in *ISVR technical memorandum No.994*. 2011, University of Southampton: Southampton.
11. Wu, T.W., ed. *Boundary Element Acoustics: Fundamentals and Computer Codes*. 2000, WIT Press: Southampton.
12. Doyle, J.F., *Wave Propagation in Structures*. 1997, New York: Springer.
13. Gavric, L., *Finite element computation of dispersion properties of thin-walled waveguides.* Journal of Sound and Vibration, 1994. **173**(1): p. 113-124.

14. Karasalo, I., *Exact finite elements for wave propagation in range-independent fluid-solid media.* Journal of Sound and Vibration, 1994. **172**(5): p. 671-688.
15. Nilsson, C.M. and S. Finnveden, *Input power to waveguides calculated by a finite element method.* Journal of Sound and Vibration, 2007. **305**(4-5): p. 641-658.
16. Kreyszig, E., *Advanced Engineering Mathematics*. 7th ed. 1993, Canada: John Wiley & Sons.
17. Morse, P.M. and K.U. Ingard, *Theoretical acoustics*. 1968, Princeton, New Jersey: Princeton University Press.
18. Pierce, A.D., *Acoustics : An Introduction to Its Physical Principles and Applications* McGraw-Hill series in mechanical engineering. 1981, New York :: McGraw-Hill Book Co.
19. Fahy, F. and P. Gardonio, *Sound and Structural Vibration: Radiation, Transmission and Response*. 2nd ed. 2006, London: Academic Press.
20. Stroud, A. and D. Secrest, *Gaussian Quadrature Formulas*. 1966, New York: Prentice-Hall.
21. Petyt, M., *Introduction to Finite Element Vibration Analysis*. 1990, Cambridge: Cambridge University Press.
22. Ih, K.D. and D.J. Lee, *Development of the direct Boundary Element method for thin bodies with general boundary conditions* Journal of Sound and Vibration, 1997. **202**(3): p. 361-373.
23. Davies, H.G., *Low frequency random excitation of water-loaded rectangular plates.* Journal of Sound and Vibration, 1971. **15**(1): p. 107-126.
24. Stepanishen, P.R., *Modal coupling in the vibration of fluid-loaded cylindrical shells.* The Journal of the Acoustical Society of America, 1982. **71**(4): p. 813-823.

Appendix A. Analytical model of sound transmission coefficient for an infinite plate strip

In [10] the sound transmission through a plate strip is calculated by ignoring cross terms. Here, the analysis is presented for the case where cross terms are retained.

The total pressure on the plate surface at $z = 0$ consists of the superposition of the blocked pressure field p_{bl} due to the incident wave and the radiated pressure field p_{rad} on both sides of the plate. The radiated pressure terms will impose a fluid loading at the plate surface. The two-dimensional bending wave equation in terms of velocity subject to the applied acoustic pressure field and the radiated acoustic pressure produced by the plate velocity is

$$D'\left(\left(\frac{\partial^4 v}{\partial x^4} + 2\frac{\partial^4 v}{\partial x^2 \partial y^2} + \frac{\partial^4 v}{\partial y^4}\right) - k_B^4 v\right) = i\omega\left(p_{bl} + p_{rad}^- - p_{rad}^+\right) \tag{A.1}$$

The distribution of the pressure $p(x, y)$ may be expressed by the combination of a Fourier integral and a Fourier series. This yields

$$p(x, y) = \frac{1}{2\pi}\int_{-\infty}^{\infty}\sum_{m=1}^{\infty} p_m(\kappa) e^{-i\kappa x} \sin\left(\frac{m\pi y}{l_y}\right) d\kappa \tag{A.2}$$

and

$$p_m(\kappa) = \frac{2}{l_y}\int_0^{l_y}\int_{-\infty}^{\infty} p(x, y) e^{i\kappa x} \sin\left(\frac{m\pi y}{l_y}\right) dx dy \tag{A.3}$$

It is assumed that the blocked pressure field consists of a reflected sound wave which is equal to the incident sound wave at the plate surface. The total pressure on the plate surface at $z = 0$ consists of the superposition of the blocked pressure field and the radiated (or scattered) pressure field due to plate motion on both sides of the plate. Hence the generalized force per unit length for mode m is given by

$$p(x,y) = 2p_i e^{-ik_y y} e^{-ik_x x} + \left(p^-_{rad}(y) - p^+_{rad}(y) \right) e^{-ik_x x} \tag{A.4}$$

and Eq. (A.3) becomes

$$p_m = \frac{2}{l_y} \int_0^{l_y} \left(2p_i e^{-ik_y y} + p^-_{rad}(y) - p^+_{rad}(y) \right) \sin\left(\frac{m\pi y}{l_y} \right) dy \left(\int_{-\infty}^{\infty} e^{i(\kappa - k_x)x} dx \right) \tag{A.5}$$

It may be noted that $\int_{-\infty}^{\infty} e^{i(\kappa - k_x)x} dx = 2\pi\delta(\kappa - k_x)$. Hence

$$p(x,y) = \sum_{m=1}^{\infty} A_m \sin\left(\frac{m\pi y}{l_y} \right) e^{-ik_x x} \tag{A.6}$$

where

$$A_m = \frac{2}{l_y} \int_0^{l_y} \left(2p_i e^{-ik_y y'} + p^-_{rad}(y') - p^+_{rad}(y') \right) \sin\left(\frac{m\pi y'}{l_y} \right) dy' \tag{A.7}$$

Similarly, because the plate strip is uniform and infinite in the $x-$direction, its transverse velocity may be written in the form

$$v(x,y) = \frac{1}{2\pi} \int_{-\infty}^{\infty} \sum_{m'=1}^{\infty} v_{m'} e^{-i\kappa x} \sin\left(\frac{m'\pi y}{l_y} \right) d\kappa \tag{A.8}$$

Using the same argument as above $\int_{-\infty}^{\infty} e^{i(\kappa - k_x)x} dx = 2\pi\delta(\kappa - k_x)$ and hence

$$v(x,y) = \sum_{m'=1}^{\infty} v_{m'} \sin\left(\frac{m'\pi y}{l_y} \right) e^{-ik_x x} \tag{A.9}$$

where m' is an integer designating each mode of the plate vibration. Eq. (A.9) can be conveniently written as

$$v(x,y) = \sum_{m'=1}^{\infty} v_{y,m'}(y) e^{-ik_x x} \tag{A.10}$$

where $v_{y,m'}(y) = v_{m'} \sin\left(m'\pi y / l_y\right)$ This transverse velocity is only defined for $0 \le y \le l_y$ and is zero otherwise. Subsequently, it can be expressed in terms of an infinite set of simple harmonic waves travelling in the $y-$ direction, with wavenumber denoted as γ in order to distinguish it from the incident wavenumber k_y, as follows

$$\tilde{V}_{y,m'}(\gamma) = \int_0^{l_y} v_{y,m'}(y) e^{i\gamma y} dy \tag{A.11}$$

$$v_{y,m'}(y) = \frac{1}{2\pi} \int_{-\infty}^{\infty} \tilde{V}_{y,m'}(\gamma) e^{-i\gamma y} d\gamma \tag{A.12}$$

The solution for $\tilde{V}_{y,m'}(\gamma)$ is

$$\tilde{V}_{y,m'}(\gamma) = v_{m'} a_{m'}(\gamma) \tag{A.13}$$

where $a_{m'}(\gamma) = \int_0^{l_y} \sin\left(\frac{m'\pi y}{l_y}\right) e^{i\gamma y} dy = \frac{(m'\pi / l_y)[(-1)^{m'} e^{i\gamma l_y} - 1]}{[\gamma^2 - \left(m'\pi / l_y\right)^2]}$

In order to solve the coupled vibration-radiation problem, some conditions must be satisfied, i.e. the fluid particle velocity must be equal to the normal plate velocity and the fluid particle velocity v and the pressure p must satisfy Euler's equation $i\omega\rho_0 \vec{v} = -\vec{\nabla} p$. Therefore, the (normal) plate velocity v in Eq. (A.10) is related to the radiated pressure by

$$v = -\frac{1}{i\omega\rho_0} \left.\frac{\partial p}{\partial z}\right|_{z=0} \tag{A.14}$$

Hence the radiated pressure field, assuming the fluid on both sides is the same, is

$$\begin{aligned} p_{rad}(x,y) &= \frac{1}{2\pi} \int_{-\infty}^{\infty} \sum_{m'=1}^{\infty} V_y(\gamma) e^{-i\gamma y} e^{-i\kappa x} \left(\frac{\omega\rho_0}{k_z}\right) d\gamma \\ &= \frac{1}{2\pi} \int_{-\infty}^{\infty} \sum_{m'=1}^{\infty} v_{m'} a_{m'}(\gamma) e^{-i\gamma y} e^{-i\kappa x} \left(\frac{\omega\rho_0}{k_z}\right) d\gamma \end{aligned} \tag{A.15}$$

or as a function of y, the radiated pressure can be written as

$$p_{rad}(y) = \frac{1}{2\pi}\int_{-\infty}^{\infty}\sum_{m'=1}^{\infty} v_{m'} a_{m'}(\gamma) e^{-i\gamma y}\left(\frac{\omega\rho_0}{k_z}\right) d\gamma \tag{A.16}$$

where $k_z = \sqrt{k^2 - \kappa^2 - \gamma^2}$. Note that $p_{rad}^{-} = -p_{rad}^{+}$.

Therefore, A_m in Eq.(A.7) becomes

$$\begin{aligned} A_m &= \frac{2}{l_y}\left(2p_i a_m(k_y) - 2\left[\frac{1}{2\pi}\left(\int_{-\infty}^{\infty}\sum_{m'=1}^{\infty} v_{m'} a_{m'}(\gamma)\left(\frac{\omega\rho_0}{k_z}\right) d\gamma\right)\left(\int_0^{l_y} e^{-i\gamma y}\sin\left(\frac{m\pi y}{l_y}\right) dy\right)\right]\right) \\ &= \frac{2}{l_y}\left(2p_i a_m(k_y) - \frac{1}{\pi}\left(\int_{-\infty}^{\infty}\sum_{m'=1}^{\infty} v_{m'} a_{m'}(\gamma) a_m^*(\gamma)\left(\frac{\omega\rho_0}{k_z}\right) d\gamma\right)\right) \end{aligned} \tag{A.17}$$

where $a_m(-\gamma) = a_m^*(\gamma)$ as the modal displacement the modal velocity function is real.

Substituting Eq. (A.6) and Eq. (A.9) into Eq. (A.1), this gives

$$\sum_{m'=1}^{\infty}\left(-\frac{i}{\omega}\left[D'\left(\left(k_x{}^2 + \left(m'\pi/l_y\right)^2\right)^2 - k_B{}^4\right)\right]\right) v_{m'} e^{-ik_x x}\sin\left(\frac{m'\pi y}{l_y}\right) = \sum_{m=1}^{\infty} A_m e^{-ik_x x}\sin\left(\frac{m\pi y}{l_y}\right) \tag{A.18}$$

Using the orthogonality of the mode shapes

$$\int_0^{l_y}\sin\left(\frac{m\pi y}{l_y}\right)\sin\left(\frac{m'\pi y}{l_y}\right) dy = \begin{cases} 0 & m \neq m' \\ \dfrac{l_y}{2} & m = m' \end{cases} \tag{A.19}$$

Eq. (A.18) can be written for a single term in the series; to obtain this, it is multiplied with $\sin\left(m\pi y/l_y\right)$ and integrated over the length l_y yielding

$$\left(-\frac{i}{\omega}\left[D'\left(\left(k_x{}^2 + \left(m\pi/l_y\right)^2\right)^2 - k_B{}^4\right)\right]\right) v_m = A_m \tag{A.20}$$

and substituting A_m from Eq. (A.17) into Eq. (A.20) after some simplifications, it is found that

$$\left(-\frac{i}{\omega}\left[D'\left(\left(k_x{}^2+\left(m\pi/l_y\right)^2\right)^2-k_B{}^4\right)\right]\right)v_m=\frac{2}{l_y}\left(p_i a_m(k_y)-2\sum_{m'=1}^{\infty}v_{m'}R_{mm'}\right) \quad \text{(A.21)}$$

where $R_{mm'}$ is the inter-modal coupling which couples the structural mode m with the radiated pressure in other modes as is given

$$R_{mm'}=\frac{1}{2\pi}\int_{-\infty}^{\infty}a_{m'}(\gamma)a_m^*(\gamma)\left(\frac{\omega\rho_0}{k_z}\right)d\gamma \quad \text{(A.22)}$$

where $k_z=\sqrt{k^2-\kappa^2-\gamma^2}$. Considering the solution of $a_m(\gamma)$, $R_{mm'}$ has non-zero values for the parity indices of odd-odd or even-even, otherwise its value is zero as the odd and even modes do not interact each other. The solution of Eq. (A.21) is rather complicated as it is not mathematically orthogonal [23, 24]. For light fluid loading, the off-diagonal terms of $R_{mm'}$ can be neglected. This implies that there is no energy transfer due to two different modes hence only direct fluid loading exists. Consequently, this removes the summation sign in second term on the right hand side of Eq. (A.21). This yields

$$v_m=\frac{4}{l_y}\frac{p_i a_m(k_y)}{\left[\left(-\frac{i}{\omega}\left[D'\left(\left(k_x{}^2+\left(m\pi/l_y\right)^2\right)^2-k_B{}^4\right)\right]\right)+\frac{4}{l_y}R_m\right]} \quad \text{(A.23)}$$

where

$$R_m=\frac{1}{2\pi}\int_{-\infty}^{\infty}\left|a_m(\gamma)\right|^2\left(\frac{\omega\rho_0}{k_z}\right)d\gamma \quad \text{(A.24)}$$

Despite the above simplification relating to fluid loading, the cross-modal radiation terms can still be included as demonstrated in next paragraphs.

The transmission coefficient τ is defined as the ratio of the transmitted sound power W_{tran} to the incident sound power W_{inc}. The sound power transmitted through the plate strip is equal to the sound power radiated into the region $z>0$, hereafter

denoted by W_{rad2}. For clarity and consistency in defining the radiated power of the plate strip, an arbitrary length of plate strip L_x is retained in the following derivation. Thus, the radiated sound power of the plate strip W_{rad2} per unit length in the $x-$direction is given by

$$W_{rad2} = \frac{1}{2}\mathrm{Re}\left\{\frac{1}{L_x}\int_{-\infty}^{\infty}\int_{0}^{L_x} p(x,y)v^*(x,y)dxdy\right\} \tag{A.25}$$

in which the range of the integration 0 to l_y has been extended to $\pm\infty$ because the form of $\tilde{V}_y(\gamma)$ ensures that v_y is zero outside $0 < y < l_y$. Substituting Eq. (A.12) and Eq. (A.15) into Eq. (A.25) for the radiated sound power per unit length, this yields

$$\begin{aligned} W_{rad2} &= \frac{1}{2}\mathrm{Re}\left\{\frac{1}{L_x}\int_{-\infty}^{\infty}\int_{0}^{L_x}\frac{1}{2\pi}\int_{-\infty}^{\infty}\frac{\rho_0 ck}{\sqrt{k^2-k_x^2-\gamma^2}}\tilde{V}_y(\gamma)e^{-i\gamma y}e^{-ik_x x}d\gamma\right. \\ &\left.\times\frac{1}{2\pi}\int_{-\infty}^{\infty}\tilde{V}_y^*(\gamma')e^{i\gamma' y}e^{ik_x x}d\gamma' dxdy\right\} \\ &= \frac{1}{4\pi}\mathrm{Re}\left\{\int_{-\infty}^{\infty}\frac{\rho_0 ck}{\sqrt{k^2-k_x^2-\gamma^2}}\tilde{V}_{y,m}(\gamma)\tilde{V}_{y,m'}^*(\gamma)d\gamma\right\} \end{aligned} \tag{A.26}$$

where $\tilde{V}_{y,m}(\gamma)$ as defined in Eq. (A.13).

Hence the total radiated sound power with the necessary condition $k_x^2+\gamma^2 \le k^2$ is

$$W_{rad2} = \frac{1}{4\pi}\sum_{m=1}^{\infty}\sum_{m'=1}^{\infty}\left\{\int_{-\sqrt{k^2-k_x^2}}^{\sqrt{k^2-k_x^2}}\frac{\rho_0 ck}{\sqrt{k^2-k_x^2-\gamma^2}}v_m a_m(\gamma)a_{m'}(\gamma)v_{m'}d\gamma\right\} \tag{A.27}$$

where the product of $a_m(\gamma)$ and $a_{m'}(\gamma)$ corresponds to the cross-modal radiation coupling.

The incident power per unit length of the plate strip can be expressed as follows

$$W_{inc} = \frac{1}{2}\frac{|p_i|^2 \cos\theta}{\rho_0 c} l_y \tag{A.28}$$

The transmission coefficient is given by

$$\tau = \frac{W_{rad\,2}}{W_{inc}} \tag{A.29}$$

Substituting Eq. (A.27) and (A.28) into Eq. (A.29) gives

$$\tau = \frac{(\rho_0 c)^2}{2\pi |p_i|^2 l_y \cos\theta} \left\{ \sum_{m=1}^{\infty} \sum_{m'=1}^{\infty} \left\{ \int_{-\sqrt{k^2-k_x^2}}^{\sqrt{k^2-k_x^2}} \frac{k}{\sqrt{k^2-k_x^2-\gamma^2}} v_m a_m(\gamma) a_{m'}(\gamma) v_{m'} d\gamma \right\} \right\} \tag{A.30}$$

The sound reduction index or transmission loss R is found from

$$R = 10\log_{10}\left(\frac{1}{\tau}\right) \quad \text{dB} \tag{A.31}$$

Note that in [10] cross terms in (A.26) were neglected leaving only a single summation. These results in a significant reduction in calculation time but yield an approximate solutions.